

How much inundation occurs in the Amazon River basin?

Ayan Santos Fleischmann ^{a,b,*}, Fabrice Papa ^{c,d}, Alice Fassoni-Andrade ^{c,d}, John M. Melack ^e, Sly Wongchuig ^f, Rodrigo Cauduro Dias Paiva ^b, Stephen K. Hamilton ^{g,y}, Etienne Fluet-Chouinard ^h, Rafael Barbedo ^b, Filipe Aires ⁱ, Ahmad Al Bitar ^j, Marie-Paule Bonnet ^k, Michael Coe ^l, Jefferson Ferreira-Ferreira ^{a,z}, Laura Hess ^e, Katherine Jensen ^{m,n}, Kyle McDonald ^{m,n}, Alex Ovando ^o, Edward Park ^p, Marie Parrens ^{j,q,r}, Sébastien Pinel ^s, Catherine Prigent ^t, Angélica F. Resende ^u, Menaka Revel ^v, Ake Rosenqvist ^w, Jessica Rosenqvist ^w, Conrado Rudorff ^o, Thiago S.F. Silva ^x, Dai Yamazaki ^v, Walter Collischonn ^b

^a Mamirauá Institute for Sustainable Development, Tefé, AM, Brazil

^b Institute of Hydraulic Research, Universidade Federal do Rio Grande do Sul (UFRGS), Porto Alegre, RS, Brazil

^c Laboratoire d'Etudes en Géophysique et Océanographie Spatiales (LEGOS), Université de Toulouse, IRD, CNRS, CNES, USP, Toulouse, France

^d Institut de Recherche pour le Développement (IRD), Universidade de Brasília (UnB), Institute of Geosciences, Campus Universitário Darcy Ribeiro, 70910-900, Brasilia, Brazil

^e Earth Research Institute, University of California, Santa Barbara, USA

^f Univ. Grenoble Alpes, IRD, CNRS, Grenoble INP, Institut des Géosciences de l'Environnement (IGE, UMR 5001), 38000 Grenoble, France

^g Kellogg Biological Station, Michigan State University, Hickory Corners, MI 49060, USA

^h Department of Earth System Science, Stanford University, Stanford, CA, USA

ⁱ Laboratoire d'Etudes du Rayonnement et de la Matière en Astrophysique et Atmosphères, Observatoire de Paris, UMR 8112, Paris, France

^j Centre d'Etudes Spatiales de la Biosphère (CESBIO), Toulouse University (CNES, CNRS, INRAE, IRD, UPS), Toulouse, France

^k Espace-DEV, Univ Montpellier, Institute of Research for Development, Univ Guyane, Univ Réunion, Montpellier, France

^l Woodwell Climate Research Center, Falmouth, MA, USA

^m Department of Earth and Atmospheric Sciences, City College of New York, City University of New York, New York, NY 10031, USA

ⁿ Department of Earth and Environmental Science, The Graduate Center, City University of New York, New York, NY 10031, USA

^o Centro Nacional de Monitoramento de Desastres Naturais (CEMADEN), São José dos Campos, São Paulo, Brazil

^p National Institute of Education, Earth Observatory of Singapore and Asian School of the Environment, Nanyang Technological University, Singapore

^q Centre d'Etudes Spatiales de la Biosphère (CESBIO), CNES, Université de Toulouse (UPS), France

^r Dynafor, Université de Toulouse, INRAE, INPT, INP-PURPAN, Castanet-Tolosan, France

^s CEFREM, University of Perpignan Via Domitia, Perpignan, France

^t CNRS, Sorbonne Université, Observatoire de Paris, Université PSL, LERMA, Paris, France

^u Universidade de São Paulo, Departamento de Ciências Florestais (ESALQ), Piracicaba, SP, Brazil

^v Institute of Industrial Science, The University of Tokyo, Tokyo, Japan

^w solo Earth Observation (soloEO), Tokyo 104-0054, Japan

^x Biological and Environmental Sciences, Faculty of Natural Sciences, University of Stirling, Stirling FK9 4LA, UK

^y Cary Institute of Ecosystem Studies, Millbrook, NY 12545, USA

^z WRI Brasil, São Paulo, Brazil

ARTICLE INFO

Edited by Menghua Wang

Keywords:

Flooding

Surface water

Floodplains

Interfluvial wetlands

ABSTRACT

The Amazon River basin harbors some of the world's largest wetland complexes, which are of major importance for biodiversity, the water cycle and climate, and human activities. Accurate estimates of inundation extent and its variations across spatial and temporal scales are therefore fundamental to understand and manage the basin's resources. More than fifty inundation estimates have been generated for this region, yet major differences exist among the datasets, and a comprehensive assessment of them is lacking. Here we present an intercomparison of 29 inundation datasets for the Amazon basin, based on remote sensing only, hydrological modeling, or multi-source datasets, with 18 covering the lowland Amazon basin (elevation <500 m, which includes most Amazon wetlands), and 11 covering individual wetland complexes (subregional datasets). Spatial resolutions range from 12.5 m to 25 km, and temporal resolution from static to monthly, spanning up to a few decades.

* Corresponding author at: Mamirauá Institute for Sustainable Development, Tefé, AM, Brazil.

E-mail addresses: ayan.fleischmann@gmail.com, ayan.fleischmann@mamiraua.org.br (A.S. Fleischmann).

Overall, 31% of the lowland basin is estimated as subject to inundation by at least one dataset. The long-term maximum inundated area across the lowland basin is estimated at $599,700 \pm 81,800 \text{ km}^2$ if considering the three higher quality SAR-based datasets, and $490,300 \pm 204,800 \text{ km}^2$ if considering all 18 datasets. However, even the highest resolution SAR-based dataset underestimates the maximum values for individual wetland complexes, suggesting a basin-scale underestimation of ~10%. The minimum inundation extent shows greater disagreements among datasets than the maximum extent: $139,300 \pm 127,800 \text{ km}^2$ for SAR-based ones and $112,392 \pm 79,300 \text{ km}^2$ for all datasets. Discrepancies arise from differences among sensors, time periods, dates of acquisition, spatial resolution, and data processing algorithms. The median total area subject to inundation in medium to large river floodplains (drainage area $> 1000 \text{ km}^2$) is $323,700 \text{ km}^2$. The highest spatial agreement is observed for floodplains dominated by open water such as along the lower Amazon River, whereas intermediate agreement is found along major vegetated floodplains fringing larger rivers (e.g., Amazon mainstem floodplain). Especially large disagreements exist among estimates for interfluvial wetlands (Llanos de Moxos, Pacaya-Samiria, Negro, Roraima), where inundation tends to be shallower and more variable in time. Our data intercomparison

Table 1

List of 29 studies that mapped inundation over areas ranging from the entire Amazon basin to individual wetland complexes. These data sources were selected based on data availability and relevance for this intercomparison. In the case of hydrological models, time resolutions are the values assessed or provided by the models, which can be provided at finer time resolution if necessary, since many of them compute flood maps at daily or sub-daily time steps and report time-integrated results. The column “Data type” refers to: OS: optical sensor; SAR: synthetic aperture radar; HM: hydrological model; HR: multiple datasets at high resolution; CR: multiple datasets at coarse resolution. The column “Type of inundation estimated” has three classes: “All”, meaning both open water and vegetated wetlands, “Open water”, and “Wetland only (no open water)”.

Data type	Dataset name and main mission/ model associated (if applicable)	Spatial resolution	Temporal resolution	Time period	Region	Type of inundation estimated	Reference
CR	GIEMS-2	25 km	Monthly	1992–2015	Basin	All	Prigent et al., 2020
CR	SWAMPS	25 km	Monthly	1992–2020	Basin	All	Jensen and McDonald, 2019
CR	WAD2M	25 km	Monthly	2000–2018	Basin	Wetland only (no open water)	Zhang et al., 2020
HR	GIEMS-D3	90 m	Monthly	1993–2007	Basin	All	Aires et al., 2017
HR	CIFOR	232 m	Static (max inundation)	1950–2000	Basin	All	Gumbrecht et al., 2017
HR	ESA-CCI	300 m	Annual	1992–2015	Basin	All	Bontemps et al., 2013
HR	GIEMS-D15	500 m	Monthly climatology	1993–2004	Basin	All	Fluet-Chouinard et al., 2015
HR	GLWD	1 km	Static	1992–2004	Basin	All	Lehner and Döll, 2004
HR	SWAF-HR/SMOS mission	1 km	Weekly to monthly	2010–2020	Basin	All	Parrens et al., 2019
HM	THMB model	5-min	Monthly	1961–2010	Basin	All	Coe et al., 2008
HM	CaMa-Flood model	500 m	Monthly	1980–2014	Basin	All	Yamazaki et al., 2011
HM	MGB model	500 m	Monthly	1980–2015	Basin	All	Siqueira et al., 2018
HM	Bonnet model	180 m	Monthly	2006–2019	Janaúacá	All	Bonnet et al., 2017
HM	TELEMAC-2D model	30 m	Monthly	2006–2015	Janaúacá	All	Pinel et al., 2019
HM	LISFLOOD-FP model	90 m	Monthly	1994–2015	Curuá	All	Rudorff et al., 2014
OS	G3WBM/Landsat mission	30 m	Static (open water areas)	1990–2010	Basin	Open water	Yamazaki et al., 2015
OS	GLAD/Landsat mission	30 m	Annual and monthly climatology	1999–2018	Basin	Open water	Pickens et al., 2020
OS	GSWO/Landsat mission	30 m	Monthly (cloud cover may occur)	1984–2019	Basin	Open water	Pekel et al., 2016
OS	Ovando/MODIS mission	500 m	8 days	2001–2014	Llanos de Moxos	Open water	Ovando et al., 2016
OS	Park/MODIS mission	230 m	Monthly climatology	2000–2015	Amazon River downstream of Manaus	Open water	Park and Latrubbles, 2019
SAR	Hess/JERS-1 mission	90 m	Max. and min. annual inundation (dual season)	1995–1996	Basin (lowlands)	All	Hess et al., 2003, 2015
SAR	Chapman/ALOS-PALSAR mission	90 m	Monthly	2006–2011	Basin	All	Chapman et al., 2015
SAR	Rosenqvist/ALOS-2 PALSAR-2	50 m	Max. and min. annual inundation (dual season)	2014–2017	Basin	All	Rosenqvist et al., 2020
SAR	Jensen/ALOS-2 PALSAR-2 mission	50 m	Irregular (26 images)	2014–2018	Pacaya-Samiria	All	Jensen et al., 2018
SAR	Arnesen/ALOS-PALSAR mission	90 m	Irregular (12 images)	2006–2010	Curuá	All	Arnesen et al., 2013
SAR	Ferreira-Ferreira/ALOS-PALSAR mission	12.5 m	Flood frequency only	2007–2010	Mamirauá	All	Ferreira-Ferreira et al., 2015
SAR	Ovando-2/ALOS-PALSAR mission	100 m	Irregular (6 images)	2006–2010	Llanos de Moxos	All	Ovando et al., 2016
SAR	Pinel-2/ALOS-PALSAR mission	30 m	Irregular (16 images)	2007–2011	Janaúacá	All	Pinel et al., 2019
SAR	Resende/ALOS-PALSAR mission	25 m	Static (max inundation)	2006–2011	Uatumá	All	de Resende et al., 2019

helps identify the current major knowledge gaps regarding inundation mapping in the Amazon and their implications for multiple applications. In the context of forthcoming hydrology-oriented satellite missions, we make recommendations for future developments of inundation estimates in the Amazon and present a WebGIS application (<https://amazon-inundation.herokuapp.com/>) we developed to provide user-friendly visualization and data acquisition of current Amazon inundation datasets.

1. Introduction

Aquatic ecosystems cover extensive areas of the Amazon basin, and are associated with temporally and spatially dynamic habitats such as floodable forests, savannas, grasslands, large and small rivers, and lakes (Hess et al., 2015; Junk et al., 2011; Melack and Coe, 2021; Reis et al., 2019). These systems, hereafter called wetlands, support plants and animals that are adapted to the flood pulse (Junk et al., 1989), play key roles in regional and global biogeochemical cycles, especially the carbon cycle (Richey et al., 1990; Dunne et al., 1998; Abril et al., 2014; Melack et al., 2004; Pangala et al., 2017; Martínez-Espinosa et al., 2020), and regulate the riverine transport of dissolved and particulate material, including sediment and organic matter (Armijos et al., 2020; Fassoni-Andrade and de Paiva, 2019; Melack and Forsberg, 2001; Ward et al., 2017). Additionally, human settlements along Amazon wetlands (Blatrix et al., 2018; Denevan, 1996) benefit from ecosystem services, including food provision from native plants and animals as well as crop and livestock production (Coomes et al., 2016; Jardim et al., 2020).

Many of the wetlands of the Amazon basin are considered floodplain because they are subject to seasonal or periodic inundation by river overflow (i.e., the flood pulse; Junk et al., 1989). The region also hosts large interfluvial wetlands, which unlike fringing floodplains along large rivers, are flooded mainly by local rainfall and runoff and characterized by shallow water (Belger et al., 2011; Bourrel et al., 2009; Junk et al., 2011). Water sources, inundation patterns, and geomorphology interact to determine the structure and function of these biodiverse ecosystems (Junk et al., 2011; Latrubblesse, 2012; Park and Latrubblesse, 2017).

The extent of inundated land (also called flooded land or surface water extent), and its temporal variation, are core variables to understand wetland processes and are of interest for multiple scientific disciplines, including ecology (Silva et al., 2013; Hawes et al., 2012; Luize et al., 2015), land-atmosphere interactions (Prigent et al., 2011; Taylor et al., 2018), carbon cycling and greenhouse gas emissions (Guilhen et al., 2020; Melack et al., 2004; Richey et al., 2002), and natural hazard management (Restrepo et al., 2020; Trigg et al., 2016). The Amazon basin has been a focus for remote sensing developments and applications in hydrology (Fassoni-Andrade et al., 2021), especially for inundation estimation, given the basin's large scale and global environmental relevance, relatively pristine landscape, and technical challenges posed by persistent cloud cover (Asner, 2001) and dense vegetation. This resulted in the development of more than 50 inundation maps and datasets for this region in recent decades. Tables 1 (datasets used in this study) and S1 (datasets not used due to redundancy or unavailability) summarize most of the datasets developed for mapping inundation in the Amazon basin.

Digital wetland maps were first produced for the Amazon basin by Matthews and Fung (1987) from aeronautical charts. Optical remote sensing systems in the visible or thermal spectral range, such as Landsat, are of limited value for most Amazon wetlands, since inundation under persistent cloud cover and dense vegetation canopies can be difficult to detect. Because of this, microwave systems have been employed. Large-scale inundation mapping was pioneered in the region through analysis of Scanning Multi-channel Microwave Radiometer (SMMR) and Special Sensor Microwave/Imager (SSM/I) passive microwave observations, which provided all-weather capability and sensitivity to inundation even in the presence of partial vegetative cover (Hamilton et al., 2002; Prigent et al., 2001; Sippel et al., 1998). Meanwhile, research demonstrated the all-weather capability and superior spatial resolution of

synthetic aperture radar (SAR) systems. L-band SAR that can penetrate forest canopies and reveal underlying water through the "double bounce" effect was shown to be promising for mapping inundation in the Amazon (Hess et al., 2003). More specifically, the high-resolution, dual-season classification of the Japanese Earth Resources Satellite-1 (JERS-1) L-band SAR data for the entire lowland Amazon basin by Hess et al. (2015), validated with airborne videography images, has been used as a benchmark for the inundation extent of Amazon wetlands. Since these initial studies, and with the availability of other imagery (e.g., Advanced Land Observing Satellite (ALOS) 1 and 2 missions), the remote sensing community seeking to map and characterize inundation employed various combinations of active and passive microwave data to benefit from the higher spatial resolution of the former and the higher temporal resolution of the latter (Aires et al., 2013; Jensen and McDonald, 2019; Papa et al., 2010; Parrens et al., 2019, 2017; Prigent et al., 2007, 2020; Schroeder et al., 2015).

Besides the basin-scale mappings (which, in our context, refer to both basin-scale datasets and those that cover only the lowland areas below 500 m.a.s.l. elevation) of annual maximum and minimum inundation (Chapman et al., 2015; Hess et al., 2015; Rosenqvist et al., 2020), dynamic datasets with high spatial and temporal resolution are mainly based on satellite passive microwave observations of coarse spatial resolution (Global Inundation Extent Multi-Satellite – GIEMS), Surface Water Microwave Product Series (SWAMPS), Surface Water Fraction (SWAF), Wetland Area and Dynamics for Methane Modeling (WAD2M) datasets; see Table 1), which can be downscaled using ancillary data (Aires et al., 2017, 2013; Parrens et al., 2019). Basin-scale, dynamic inundation estimates based on the ALOS satellite are limited given its low temporal resolution (repeat cycle of 46 days). Thus, some studies have analyzed time series of ALOS-Phased Array L-band Synthetic Aperture Radar (PALSAR) (Arnesen et al., 2013; Ferreira-Ferreira et al., 2015) and ALOS-2 PALSAR-2 backscatter retrievals (Jensen et al., 2018) for subsets of Amazon wetlands. However, with a few exceptions using subregional datasets (Arnesen et al., 2013; Ferreira-Ferreira et al., 2015; Hess et al., 2003; Jensen et al., 2018; de Resende et al., 2019), in situ validation of the basin-scale estimates has seldom been performed, given the remoteness of much of the Amazon basin and the often dense forest cover, which hampers airborne monitoring of below-canopy inundation.

Complementary to the remotely sensed datasets, process-based hydrological models estimating variables such as river discharge and flood extent have been developed and assessed from basin to local scales in the major rivers of the basin (Beighley et al., 2009; Coe et al., 2008; Getirana et al., 2017, 2012; Hoch et al., 2017; Luo et al., 2017; Miguez-Macho and Fan, 2012; Paiva et al., 2013; Yamazaki et al., 2011), thanks to the advent of new computational and modeling capabilities. Local-scale hydraulic models with coarse (Trigg et al., 2009; Wilson et al., 2007; Fleischmann et al., 2020) and detailed input data (Ji et al., 2019; Pinel et al., 2019; Rudorff et al., 2014; Fassoni-Andrade, 2020) have further developed model capabilities for mapping inundation dynamics, especially for the floodplains fringing the Amazon mainstem. These models complement satellite-based flood mapping due to their higher temporal and spatial resolution, and capability to estimate long-term time series, for both past and future (e.g., due to climate change) scenarios. The understanding of their uncertainties can lead to optimal data fusion with satellite-based estimates, such as considering multiple constraints within the water cycle representation (Pellet et al., 2021).

Among these numerous inundation datasets for the Amazon basin (Tables 1 and S1), divergences can be substantial due to the differences

in sensor systems, timing, and data processing algorithms (Aires et al., 2018; Fleischmann et al., 2020; Parrens et al., 2019; Pham-Duc et al., 2017; Rosenqvist et al., 2020), and a comprehensive assessment of inundation estimates for the Amazon is lacking. The need to compare different hydrological datasets for the Amazon has been recently highlighted in the context of river discharge (Towner et al., 2019), precipitation (Wongchug et al., 2017; Zubeta et al., 2019) and evapotranspiration (da Paca et al., 2019; Wu et al., 2020). Meanwhile, rapid environmental changes in the basin underscore the urgency for a better understanding of Amazon water resources (Fassoni-Andrade et al., 2021), for which management and planning can be hindered by the discrepancies among datasets. These questions regarding current data limitations in the largest basin in the world are also timely in anticipation of forthcoming hydrological satellite missions such as Surface Water and Ocean Topography (SWOT) and NASA-ISRO SAR (NISAR).

To better understand and quantify the state of understanding of

inundation patterns in the Amazon wetlands, we address the following questions: 1) How much Amazon land area is subject to seasonal or permanent flooding, and how accurate are the estimates? 2) Which areas are in particular disagreement and thus deserve further attention? 3) How do basin-scale estimates with coarser resolution and less calibrated classification methods differ from those for individual wetland complexes, with independent validation? 4) How do the various inundation estimation approaches (optical imagery, SAR, passive microwave, hydrologic models) differ in terms of inundation mapping and for different wetland types (e.g., floodplains and interfluvial areas)? In order to answer these questions, we gathered 29 inundation datasets for the Amazon basin, spanning a wide range of spatial (12.5 m to 25 km) and temporal (static, dual-season, monthly, daily) resolutions, and coverages from the whole basin to individual wetland complexes (Table 1), into a framework that provides a comprehensive assessment of current knowledge of Amazon inundation.

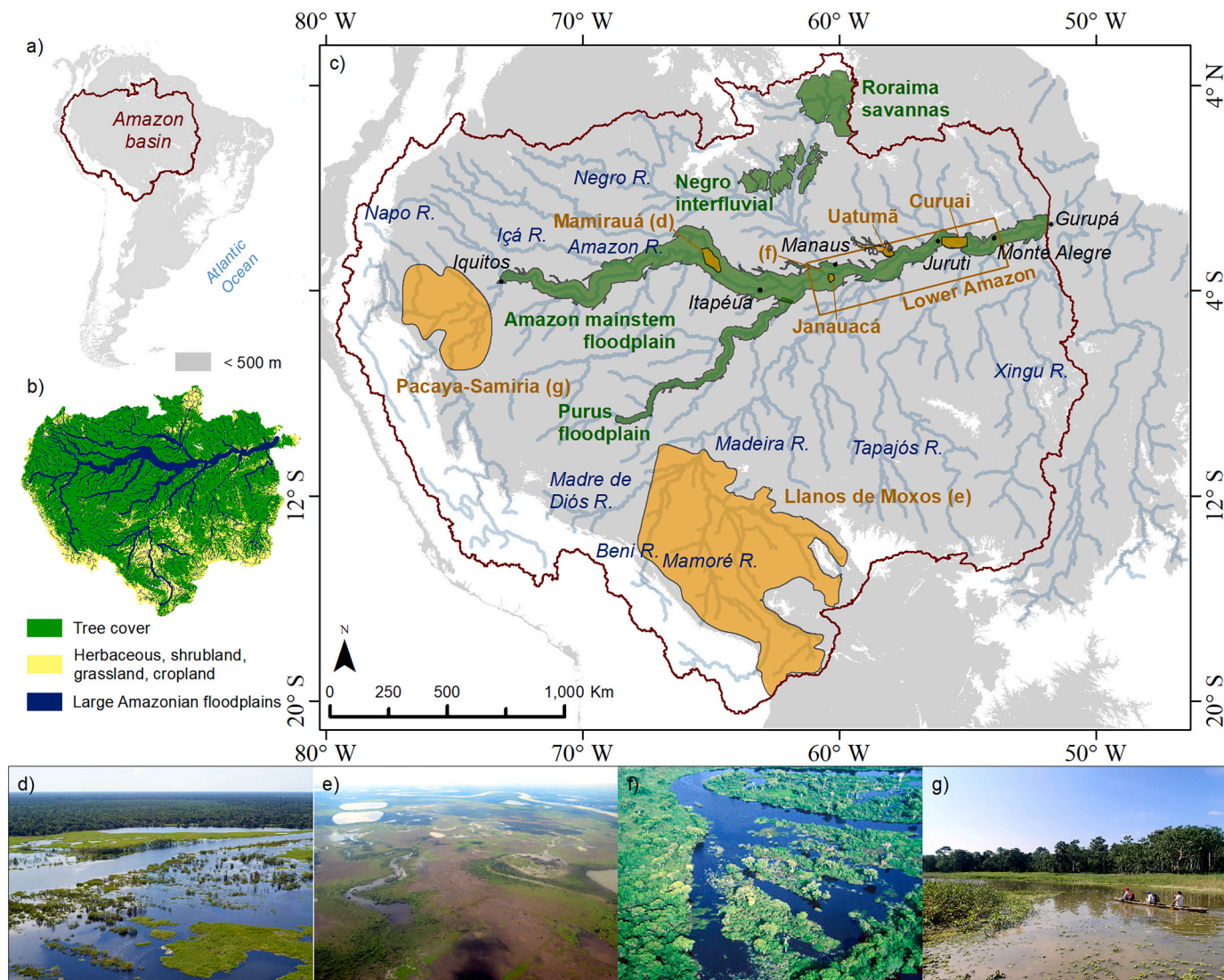


Fig. 1. The Amazon basin and its major wetland systems: (a) Amazon basin delineation (red lines) over the countries of South America (black lines). (b) Land cover based on a 2010 map from the European Space Agency Climate Change Initiative (ESA-CCI) (Bontemps et al., 2013), showing the distribution of forest and non-forest cover across the basin, as well as large floodplains (see methodology section 2.3). (c) Basin distribution of major wetland systems showing locations of interest for this study. Elevations lower than 500 m are shown in grey (based on SRTM DEM). The orange polygons show the areas for which a subregional dataset was available for this study (Fig. 4), and the green ones show wetland areas of interest that do not have datasets specifically designed for these subregions. Photos depicting different wetland complexes for (d) Mamirauá (courtesy of João Paulo Borges Pedro), (e) Llanos de Moxos (courtesy of Alex Ovando), (f) Cabaliana floodplain lake close to Manacapuru (courtesy of Stephen Hamilton), and (g) Pacaya-Samiria (courtesy of Katherine Jensen) regions, respectively. (For interpretation of the references to colour in this figure legend, the reader is referred to the web version of this article.)

2. Methodology

2.1. Study area

The Amazon basin spans around 6 million km² in nine South American countries (Fig. 1), with high annual rainfall (~2200 mm year⁻¹), and the Amazon River discharge makes a major contribution to global freshwater and sediment exports to the ocean (Fassoni-Andrade et al., 2021). We delineated the catchment area upstream from Gurupá city, within the tidal river ~390 km from the ocean; hence not including the Tocantins-Araguaia basin and parts of the Amazon estuary and Marajó Island. We selected the 5.11×10^6 km² of Amazon lowlands defined as areas lower than 500 m elevation based on the Shuttle Radar Topography Mission Digital Elevation Model (SRTM DEM) for the area of dataset comparisons in our study. This decision is consistent with several studies limited to lowlands because of the limitations of certain methods in estimating flooding in mountainous terrain (Hess et al., 2015).

In addition to basin-scale datasets, estimates of inundated areas for 11 individual wetland complexes (also referred to as “subregional”) in the Amazon basin were analyzed, including seven areas for which more detailed estimates were available. This was performed to understand how the basin-scale datasets may vary in accuracy across different wetland types (Fig. 1): Curuai floodplain lake (Arnesen et al., 2013; Rudorff et al., 2014), Janauacá floodplain lake (Bonnet et al., 2017; Pinel et al., 2019), Uatumã river floodplain (de Resende et al., 2019), Mamirauá Reserve (Ferreira-Ferreira et al., 2015), Pacaya-Samiria wetlands (Jensen et al., 2018), Llanos de Moxos wetlands (Ovando et al., 2016), lower Amazon floodplain (Park and Latrubesse, 2019), Amazon mainstem floodplain (from Iquitos to Gurupá), Purus floodplain, Roraima savannas, and Negro campinas and campinaranas. A brief summary of these wetlands is provided in supplementary Table S2, and their main features are summarized in the following. Curuai is representative of the shallow lakes in the lower Amazon floodplain. It is separated from the river by narrow levees (Rudorff et al., 2014) and has a high suspended sediment concentration. Janauacá is typical of the middle Amazon River floodplain, and is composed of a ria lake (i.e., a blocked valley lake with relatively sediment-free waters; Latrubesse (2012)) and “várzea” environments (white-water floodplains) in its northern part (Pinel et al., 2019). Uatumã River is an Amazon tributary with black-water floodplain (“igapó”), and includes the Balbina hydroelectric reservoir, operating since 1987, which affects the river’s hydrological regime (Schöngart et al., 2021). The Uatumã floodplain reach assessed here is the 300-km reach between Balbina dam and the confluence with the Amazon River. The Mamirauá Sustainable Development Reserve is located in the confluence between Solimões and Japurá rivers, and is characterized by a mosaic of “chavascal”, herbaceous, and low and high várzea vegetation (Ferreira-Ferreira et al., 2015). The Purus River is a major tributary, and its floodplain was chosen because of its large floodplain to river width ratio. Pacaya-Samiria wetlands are composed of flooded forests, palm swamps and peatlands in the upper Solimões River (Draper et al., 2014; Läheenoja et al., 2012). The Llanos de Moxos floodable savannas occupy the interfluvial areas between the Beni, Mamoré and Madre de Dios rivers in the upper Madeira basin (Hamilton et al., 2004). The Negro’s interfluvial wetland vegetation, locally known as “campinas” (herbaceous vegetation) and “campinaranas” (mixed herbaceous and arboreal vegetation), are thought to have formed from regional neotectonic depressions and were called the “Septentrional Pantanal” given their large area (Rossetti et al., 2017a, 2017; Santos et al., 1993). The Roraima floodable savannas extend from Roraima State in Brazil to the Rupununi savannas in Guyana, and comprise mainly smaller river floodplains interspersed with poorly drained interfluvial savannas subject to flooding by local rainfall (Hamilton et al., 2002); here we only considered the Roraima wetlands in the upper Branco River basin, which is within the Amazon basin.

2.2. Datasets

Twenty-nine inundation datasets covering areas ranging from the whole-basin scale to individual wetland complexes, based on multiple data sources and spatiotemporal resolutions, were assembled for our comparison (Table 1). Most of these datasets are recent, with 18 out of the 29 published since 2016, and 27 since 2011. They were chosen due to data availability and representativeness; other datasets that were either unavailable or methodologically redundant to those in our comparison were not used but are catalogued in Table S1. Overall, there are eight dynamic (weekly to monthly; Fig. 2) and 10 static (which include long-term maximum, annual or dual-season categories; Fig. 3) basin-scale datasets.

Passive microwave (PM) data are the basis of SWAF-HR, GIEMS family (GIEMS-D15, GIEMS-D3, GIEMS-2), and SWAMPS, while ancillary data (i.e., optical imagery and microwave scatterometry) are used to complement the PM signal. SWAF-HR data result from the disaggregation of water surface fraction in a dataset at coarser spatial resolution (SWAF), based on L-band passive microwave observations from the Soil Moisture and Ocean Salinity (SMOS) satellite (Parrens et al., 2017). The disaggregation of SWAF relies on water occurrence maps from GSOW and the Digital Elevation Model (DEM) Multi-Error-Removed-Improved-Terrain (MERIT) (Parrens et al., 2019). A global implementation of SWAF based on multi-angular and multi-polarization information has also been implemented (Al Bitar et al., 2020). GIEMS merges multiple satellite passive and active microwave observations, along with the optically-derived NDVI (Normalized Difference Vegetation Index), to detect the surface water and estimate the vegetation attenuation, for a monthly quantification of the surface water extent at ~25 km spatial resolution (Prigent et al., 2001, 2007, 2020; Papa et al., 2010). It is further disaggregated at 90-m resolution (GIEMS-D3) using a topographical downscaling methodology (Aires et al., 2017).

Three basin-scale datasets are based mainly on SAR data from JERS-1 (Hess et al., 2003, 2015), and its successor missions ALOS-PALSAR (Chapman et al., 2015) and ALOS-2 PALSAR-2 (Rosenqvist et al., 2020). These three datasets cover different decades of observation but are methodologically similar.

Three of the optical-based datasets are based on Landsat data: GSOW (Pekel et al., 2016), G3WBM (Yamazaki et al., 2015) and GLAD (Pickens et al., 2020). Although GSOW and GLAD can provide monthly estimates for the Landsat archive (1984-today), given the inability of optical data to estimate flooding under cloud cover or dense vegetation canopies, only annual maximum and minimum values are used. For GLAD and GSOW, we consider a threshold of occurrence of surface water of 95% to estimate the minimum inundation (i.e., for the permanently inundated areas; Aires et al., 2018); otherwise, only a few isolated open water areas would be considered for the minimum extent.

The European Space Agency Climate Change Initiative dataset (ESA-CCI) is based on surface reflectance from MERIS, the Advanced Very High-Resolution Radiometer (AVHRR) and PROBA-V data and Global Water Bodies from the Envisat Advanced Synthetic Aperture Radar (ASAR) (Bontemps et al., 2013). Since the wetland pixels in ESA-CCI varied negligibly throughout the years of observations, we use only the 2010 dataset as the ESA-CCI estimate for maximum inundation.

Another set of data is based on the merging of multiple global datasets: GLWD, GIEMS-D15 and WAD2M. GLWD is one of the first globally consistent databases of wetlands, which was based on a collection of wetland estimates from diverse institutions worldwide (Lehner and Döll, 2004). GIEMS-D15 combines GLWD, the Hydrosheds drainage network, and Global Land Cover 2000. WAD2M is based on SWAMPS and CIFOR within its merging framework. WAD2M is the only dataset to exclude open water areas (removal based on GSOW) due to its goal of estimating wetland methane emissions. SWAF-HR (Parrens et al., 2019) and GIEMS-D3 (Aires et al., 2017) use additional data and methodologies to downscale the original 25-km passive microwave-based SWAF (Parrens et al., 2017) and GIEMS (Papa et al., 2010;

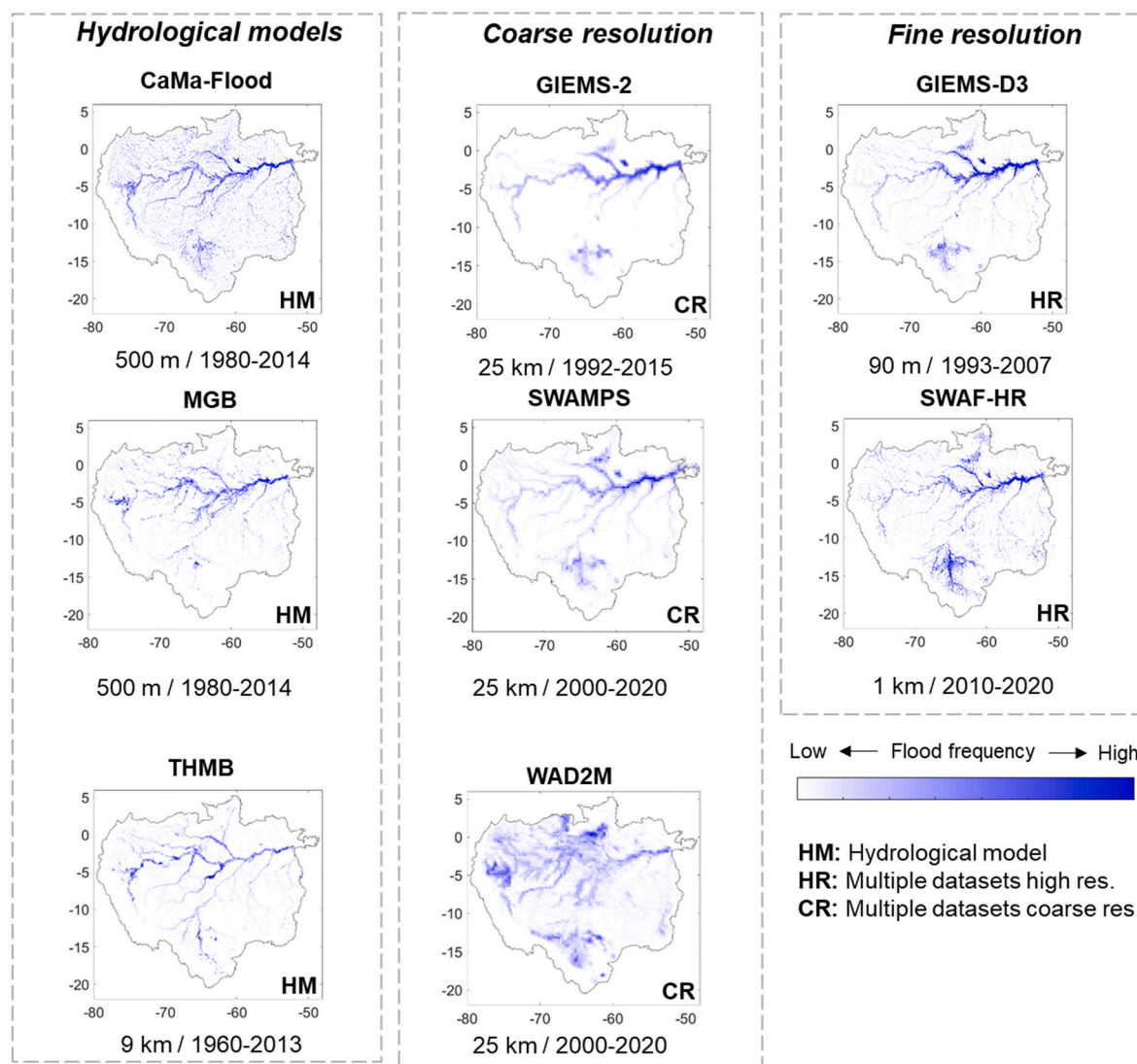


Fig. 2. Basin-scale, dynamic inundation datasets used in this study, divided into three classes (hydrological models; merging of multiple datasets at high resolution; merging of multiple datasets at coarse resolution). Long-term flood frequency maps are provided for each dataset, calculated as the percentages of observations labelled as flooded throughout the entire time-series.

Prigent et al., 2007) datasets to 1 km and 90 m, respectively. While GIEMS-D3 has a different inundation magnitude than the original GIEMS due to merging with ancillary data, SWAF-HR conserves the same inundation magnitude across scales.

Among hydrological models, we selected representative datasets from each of the following broad modeling types: 1) process-based hydrologic models that use flood routing to represent inundation processes (i.e., from a simple kinematic wave model coupled to an inundation method to more complex flow routing methods); or 2) hydraulic (or hydrodynamic) models that consider the shallow water equations (or its simplifications) at any dimension (1D, 2D or 3D). For our analysis, we adopted two basin-scale models – one hydrologic (THMB; Coe et al. (2008)) and one hydrologic-hydrodynamic (MGB, Siqueira et al. (2018)), as well as a global-scale hydrodynamic model (CaMa-Flood, Yamazaki et al. (2011)), in the Earth2Observe version available at <<http://www.earth2observe.eu/>>). The inundated area estimation is largely affected by the DEMs. The DEMs adopted in the model runs were: Bare-Earth (O'Loughlin et al., 2016) for MGB, MERIT (Yamazaki et al., 2017) for CaMa-Flood, and SRTM (Farr et al., 2007) for THMB. The rainfall/runoff input data are MSWEP v.1.1 daily precipitation (Beck et al., 2017) for MGB, HTESEL daily runoff (Balsamo et al., 2009) for

CaMa-Flood, and CRU TS v.3.2.1 monthly precipitation (Harris et al., 2014) for THMB. Although other hydrologic models have been applied to the Amazon basin (Tables 1 and S1), the models chosen here were selected as representative of global to local models, for having been well validated and applied over the Amazon basin, and for representing state-of-the-art Amazon hydrologic modeling. All basin-scale models represent one-dimensional (1D) flows only (i.e., floodplains are represented as storage units without active flow), and thus do not represent 2D surface flows that occur in wetlands (Alsdorf et al., 2007; Fleischmann et al., 2020). A detailed comparison of model capabilities and structural uncertainties is beyond our current scope. Hydrologic models have different temporal resolution depending on their numerical stability and forcing data. For instance, MGB and CaMa-Flood models run at an adaptive time step (sub-minute timestep in the case of MGB), but are assessed at daily resolution given their daily precipitation forcing. We aggregated the models' estimates to monthly averages to make them comparable to the remote sensing dynamic datasets.

The datasets available for individual wetland complexes are presented in Fig. 4. ALOS-2 PALSAR-2 data were used for the Pacaya-Samiria region (Jensen et al., 2018), and the ScanSAR mode of ALOS/PALSAR for the following datasets: Curuai floodplain lake (Arnesen

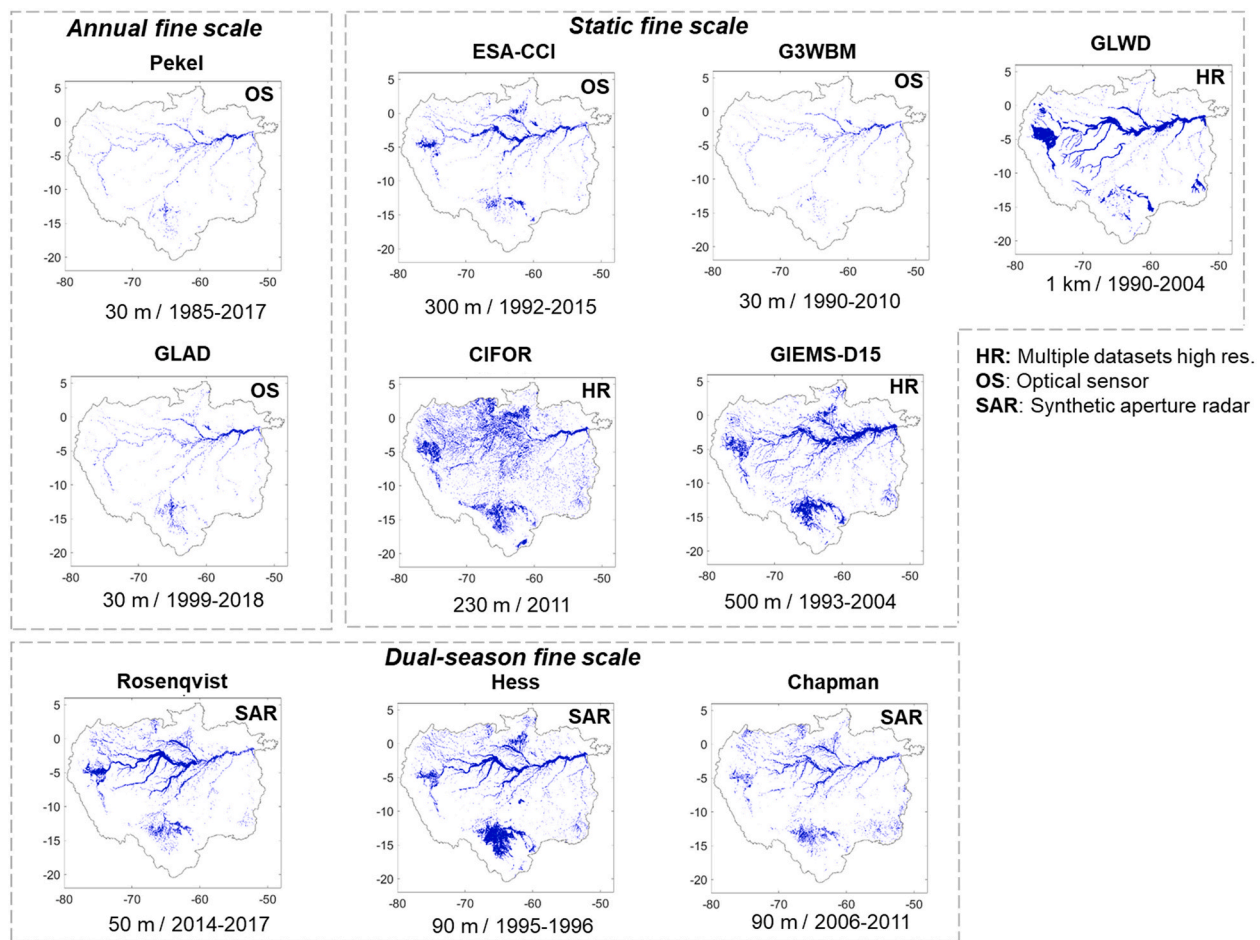


Fig. 3. Basin-scale, static or dual-season inundation datasets used in this study, divided into three classes (merging of multiple datasets at high resolution; based on optical sensors; and based on SAR data). Flood frequency maps are not provided because the datasets are mainly static or annual-based.

et al., 2013), Mamirauá Reserve (Ferreira-Ferreira et al., 2015), Uatumã river floodplain (de Resende et al., 2019), and Janaúacá floodplain lake (Pinel et al., 2019). MODIS optical data were used for the Llanos de Moxos savannas in the upper Madeira River basin (Ovando et al., 2016) and the lower Amazon floodplain (Park and Latrubblesse, 2019). Two local-scale 2D hydraulic models (LISFLOOD-FP for Curuáí lake, Rudorff et al. (2014), and TELEMAC-2D for Janaúacá lake, Pinel et al. (2019)), and one local-scale hydrologic model (for Janaúacá lake; Bonnet et al. (2017)) were considered; together, these are representative of the state-of-the-art of hydrological modeling in Amazon wetlands.

The datasets were stored in various formats (i.e., raster and polygon shapefiles) and projections (mainly projected UTM and geographic coordinate system with WGS84 datum), and were converted to the WGS84 geographic coordinate system to compute areas. SWAMPS was provided at the Equal-Area Scalable Earth (EASE) Grid, which was used to estimate its flooded areas. Hydrologic model outputs were provided as either binary inundation maps or flood depth raster files, which were then converted into binary maps by assuming depth > 0 m as inundated pixels.

2.3. Comparison framework

The comparison framework involved the following analyses, considering the entire basin and 11 wetland complexes (seven areas with available subregional estimates, and four additional areas of interest without subregional estimates; Fig. 1):

- Annual maximum and minimum inundation estimates for each of the 18 basin-scale datasets (section 3.1);
- Basin-scale, long-term maximum and minimum inundation estimates for each of the 18 basin-scale datasets (section 3.1);
- Long-term maximum and minimum inundation estimates for each of the 18 basin-scale and 11 subregional datasets (section 3.2);
- Comparison between basin-scale and subregional datasets with temporal (nRMSE and Pearson correlation) and spatial (Fit metric) assessment (section 3.2);
- Assessment of spatial agreement among the 18 basin-scale datasets at 1 km, for both long-term maximum and minimum inundation maps (section 3.3);
- Estimation of long-term maximum inundation for two classes of wetlands for the entire basin: (i) medium to large river floodplains and (ii) interfluvial wetlands and small floodplains (section 3.4).

The long-term maximum and minimum inundation extents were computed for each dataset as the area of all pixels that were inundated at least once in the whole monthly time series, for the maximum, and as those pixels that were always inundated, for the minimum. We stress that analyzing long-term changes in inundation patterns is beyond the scope of this study, and thus we assumed stationarity in our comparisons of long-term maximum and minimum inundation extents from different time-periods.

The agreement of all basin-scale, high-resolution datasets (i.e., all basin-scale ones except for THMB, GIEMS-2, SWAMPS and WAD2M, which have a coarse resolution between 9 and 25 km) was assessed for long-term maximum and minimum inundation at 1 km resolution,

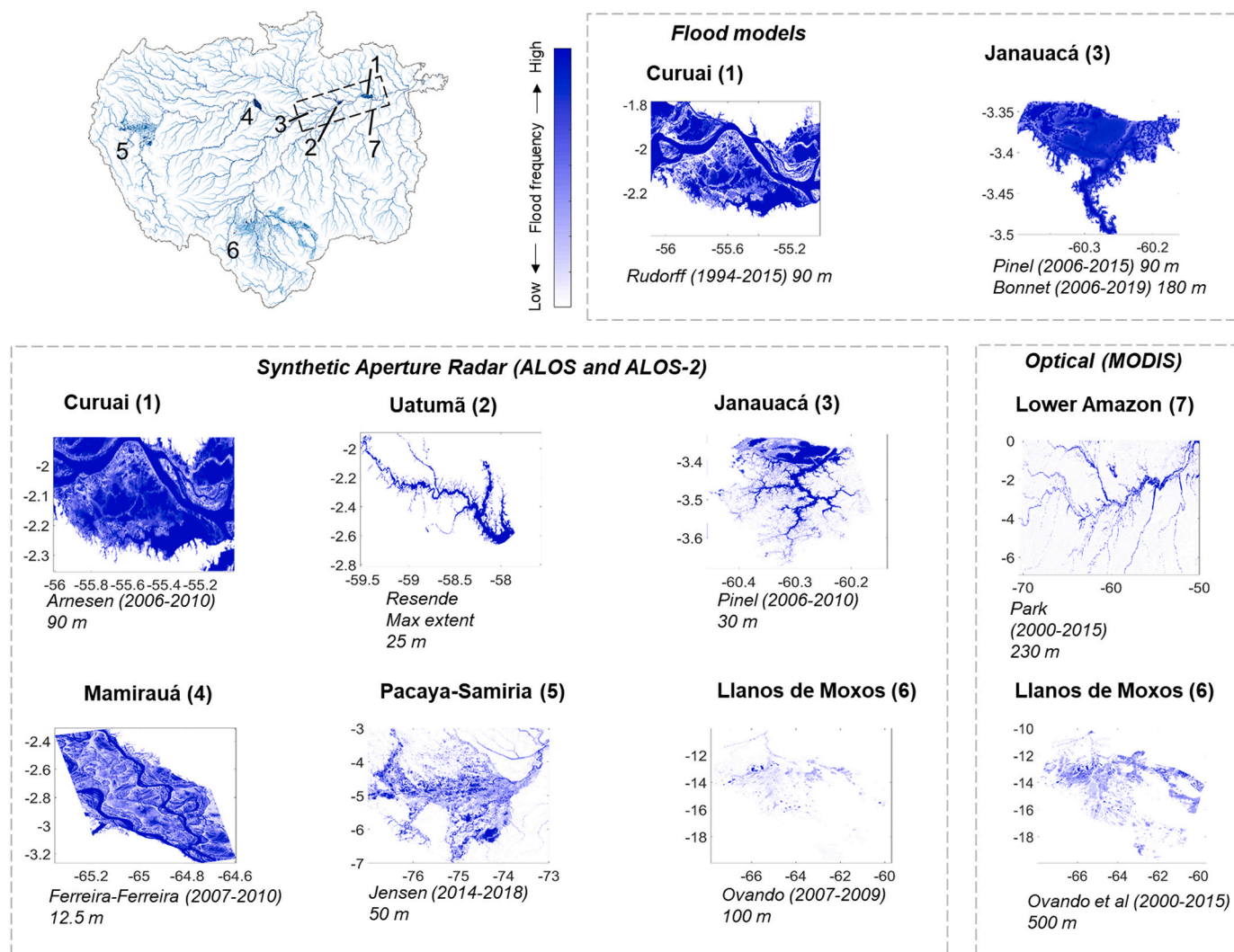


Fig. 4. Long-term flood frequency maps from subregional inundation datasets (i.e., for individual wetland complexes) used in this study. The Uatumá dataset (2) is static and is displayed as the maximum extent. Flood frequency maps are produced by computing the long-term average of all inundation maps available for each dataset.

which is the resolution of SWAF-HR, the coarsest resolution among the high-resolution datasets. For each 1 km pixel, the total number of datasets agreeing that it was inundated (either for maximum or minimum extent) was computed, following Trigg et al. (2016). Given the size of the Amazon basin, a 1 km resolution was considered adequate for the analysis. The analysis was done by aggregating all datasets to 1 km, and considering that a 1 km pixel is flooded if more than 50% of its area is flooded (following Hamilton et al., 2002). A sensitivity test was performed using a 25% threshold and led to similar conclusions at the whole basin scale (Fig. S1).

The basin-scale and four additional subregional datasets were compared to seven subregional ones, which were used as independent validation datasets, and cover the following sites: Curuá (Arnesen et al., 2013), Uatumá (de Resende et al., 2019), Janauacá (Pinel et al., 2019), Mamirauá (Ferreira-Ferreira et al., 2015), Pacaya-Samiria (Jensen et al., 2018), Llanos de Moxos MODIS (Ovando et al., 2016) and lower Amazon River (Park and Latrubblesse, 2019). Varying degrees of validation exercises were performed for these validation datasets, with some being extensively validated with airborne videography (Hess et al., 2003) or local surveys (Arnesen et al., 2013; Ferreira-Ferreira et al., 2015; Jensen et al., 2018; de Resende et al., 2019), while others were assessed through comparisons with other datasets (Pinel et al., 2019), or visually inspected, as in the large domains of the Llanos de Moxos (Ovando et al.,

2016) and lower Amazon River (Park and Latrubblesse, 2019) subregional datasets. The four additional subregional datasets are: Curuá LISFLOOD-FP model (Rudorff et al., 2014), Janauacá hydrological model (Bonnet et al., 2017), Janauacá TELEMAC-2D model (Pinel et al., 2019), and Llanos de Moxos ALOS-PALSAR (Ovando et al., 2016).

To use the subregional studies to assess the accuracy of the datasets covering broader areas, the basin-scale and four additional subregional datasets were compared to the subregional validation datasets at monthly temporal resolution, considering the total inundated area per wetland area (i.e., the whole Curuá Lake domain, the whole Uatumá floodplain, and so forth). The polygons of each wetland area, which were used to extract the information from the basin-scale datasets, were delineated as a 1-km buffer around the maximum inundated area, according to each subregional dataset. For the four areas of interest without subregional datasets (Amazon mainstem and Purus floodplains, and Roraima and Negro wetlands), the polygons were created considering the maximum lateral extent in accordance with the MERIT DEM (Yamazaki et al., 2017) and ESA-CCI land cover for savannas. The time series were compared with Pearson linear correlation (R) and the normalized root mean square deviation (nRMSD), computed as the RMSD between a given inundation map and the subregional validation map (i.e., the individual wetland complexes) divided by the subregional long-term average inundation. The term 'deviation' was preferred over

'error' to stress the uncertainties inherent to all datasets, for both basin and subregional scales, although those derived for an individual wetland complex are considered as superior in accuracy for having a more dedicated data processing for that particular area, and being validated with ground surveys in some cases.

The ability of a particular dataset to estimate the local spatial patterns at maximum inundation was assessed with the Fit metric (Bates and De Roo, 2000), which has been successfully applied to compare inundation datasets (Bernhofen et al., 2018), and is computed as:

$$Fit = 100\% * \frac{A \cap B}{A \cup B} \quad (1)$$

Where A and B are the subregional validation dataset estimates (e.g., the subregional map that corresponds to maximum inundation) and the basin-scale maximum inundation maps.

To assess different wetland environments, we differentiate medium to large river floodplains from interfluvial wetlands and small floodplains. An estimation of the total flooded area of large river floodplains was computed, considering river reaches with upstream drainage area larger than 1000 km^2 , and a buffer mask around the river reaches (mask presented in Fig. 1). The buffer was defined based on the Hydrosheds drainage network (Lehner and Grill, 2013), segmented into 15 km-long reaches as in Siqueira et al. (2018). The buffer was proportional to the local reach drainage area and further manually adjusted to include the maximum floodplain lateral extent, as estimated from a visual inspection of the MERIT DEM (Yamazaki et al., 2017) and the three basin-scale SAR-based datasets (Hess, Chapman and Rosenqvist datasets). Buffer

values varied from 4 km in upper reaches to 150 km on the Amazon mainstem close to the Mamirauá Reserve. Estimating floodplain total inundated area is relevant to differentiate the Amazon riverine fringing floodplains from non-floodplain wetlands (here referred to as interfluvial wetlands).

Finally, in order to assess the current capabilities of basin-scale mapping of inundation dynamics at high spatial and temporal resolution, a further assessment of the four high-resolution dynamic datasets (GIEMS-D3, CaMa-Flood, SWAF-HR and MGB) at their native resolutions was performed by computing their long-term flood frequency for the entire basin.

3. Results and discussion

3.1. How much inundation is estimated to occur in the Amazon basin?

3.1.1. Overall assessment

Comparisons among the various estimates of inundation area can begin with the maximum and minimum inundated area across the entire Amazon basin. We found wide variation in the annual maximum and minimum inundation estimates for the entire basin scale (Fig. 5), as well as the long-term maxima and minima (Fig. 6 and Table 2). The annual maximum inundation area represents the total area subject to inundation at some point over the year, whereas the annual minimum inundation area represents the area that remained inundated all year. SAR estimates, especially those based on L-band sensors and those having undergone validation (i.e., the Hess et al. (2003) dataset), are assumed

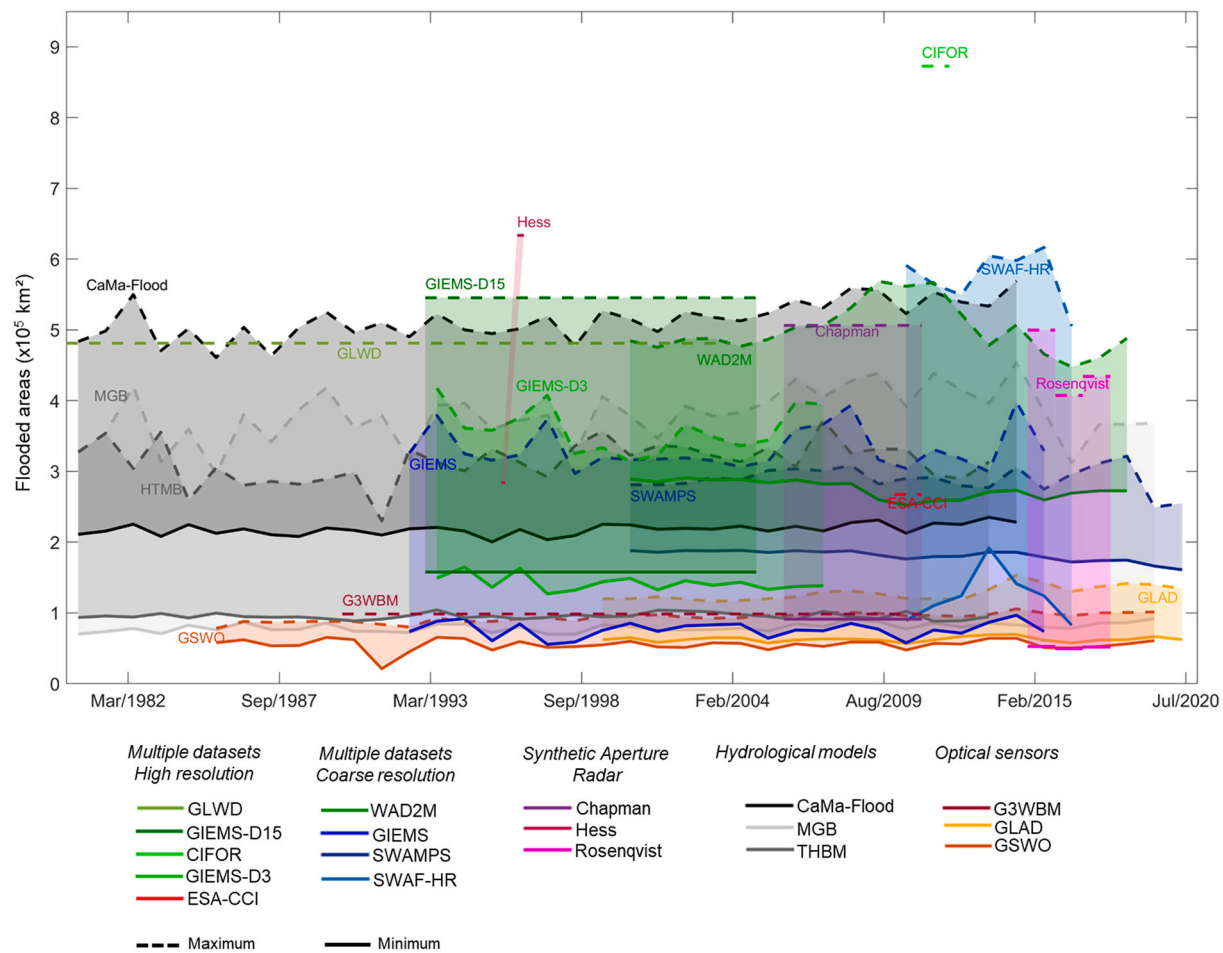


Fig. 5. (a) Annual maximum and minimum flooded areas for the Amazon basin (< 500 m in elevation) for 18 basin-scale datasets over their respective observation time periods. Note that some datasets provide only average estimates based on multiple years of observation (e.g., GLWD, Chapman, G3WBM), and are marked as horizontal lines for the period of observation.

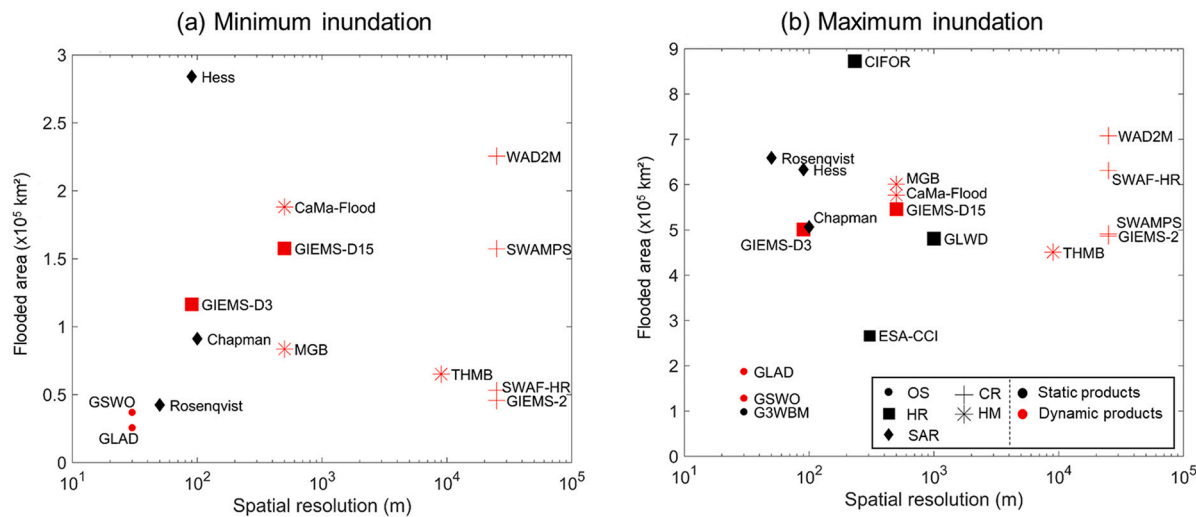


Fig. 6. Summary of long-term (a) minimum and (b) maximum inundation for the 18 basin-scale datasets, which are categorized into five types (optical data; combination of datasets at high resolution; combination of datasets at low resolution; synthetic aperture radar; and hydrological models). Estimates by dynamic datasets are not directly comparable to the static ones; thus, each is colored differently: red (dynamic) and black (static). Legend for dataset types: OS: Optical Sensor; SAR: Synthetic Aperture Radar; HM: Hydrological Model; HR: multiple datasets at High Resolution; CR: multiple datasets at Coarse Resolution. (For interpretation of the references to colour in this figure legend, the reader is referred to the web version of this article.)

Table 2

Basin-scale, long-term minimum and maximum inundation estimates for 18 datasets.

	Dataset	Minimum (km ²)	Maximum (km ²)
Multiple datasets at coarse resolution	GIEMS-2	45,800	486,600
	SWAMPS	157,400	491,100
Multiple datasets at high resolution	WAD2M	225,500	707,900
	GIEMS-D3	116,600	500,700
Hydrological model	CIFOR	–	872,700
	ESA-CCI	–	267,400
	GIEMS-D15	157,700	545,400
	GLWD	–	481,200
	SWAF-HR	53,200	630,900
	THMB	65,200	450,800
	CaMa-Flood	188,100	576,700
	MGB	83,600	600,900
Optical sensor	G3WBM	–	98,500
	GLAD	25,700	187,600
	GSWO	37,000	128,500
	Hess	284,200	633,500
Synthetic Aperture Radar	Chapman	91,200	506,400
	Rosenqvist	42,400	659,100

to be the most accurate given their high spatial resolution and capability of mapping flooded areas under dense vegetation canopies and cloud cover. Given the lack of ground validation for most basin-scale datasets, we assess their accuracy by comparing them to subregional validation datasets in section 3.2.

By computing means and standard deviations of the long-term maximum area subject to inundation by type of data (Table 2), we obtain the following values: $138,200 \pm 45,300 \text{ km}^2$ (mean \pm S.D.) for optical, $533,500 \pm 217,800 \text{ km}^2$ for multiple datasets at high resolution, $579,100 \pm 108,900 \text{ km}^2$ for those at coarse resolution, $542,800 \pm 80,600 \text{ km}^2$ for hydrological models, and $599,700 \pm 81,800 \text{ km}^2$ for SAR. The mean area for optical-based datasets is thus around 23% of the SAR-based estimate. If we assume that the ensemble of datasets could be a proxy of inundation uncertainty in the Amazon basin, and neglecting the optical and land cover-based data (G3WBM, GLAD, GSWO and ESA-CCI) and CIFOR datasets, given their lower capability to map inundation as discussed below, 13 datasets are left, yielding an estimation for the

long-term maximum inundation of $559,300 \pm 81,100 \text{ km}^2$. This value is around $40,000 \text{ km}^2$ lower than the mean of the maximum inundation area from the three SAR datasets. The mean of the maximum inundation area considering all 18 datasets is $490,300 \pm 204,800 \text{ km}^2$. Compared to the maximum inundation area, the relative deviation among available estimates is higher for the long-term minimum area inundated — $125,900 \pm 77,600 \text{ km}^2$ (mean \pm S.D.), with a coefficient of variation of 0.62, for the 12 basin-scale datasets that provide minimum area, and $139,300 \pm 127,800 \text{ km}^2$ for the three SAR-based datasets, with a coefficient of variation of 0.92.

None of the datasets can map small, narrow floodplains or riparian zones, for which only simple calculations are currently available (e.g., Junk et al., 1993), and whose total area can only be estimated through statistical extrapolation of observable rivers. These small zones contribute to the overall uncertainties of the inundation estimates. For instance, a wetland mask developed by Hess et al. (2015) for SAR-based wetland classification yielded a basin-scale estimation of wetland area including the smallest floodplains of $840,000 \text{ km}^2$. This estimate is much larger than the largest long-term maximum inundated area obtained with SAR data ($659,100 \text{ km}^2$ with Rosenqvist's dataset). In section 3.2, it will be shown that almost all datasets tend to underestimate the maximum inundation, when compared to subregional ones. The two SAR-based datasets with highest accuracy underestimate maximum inundation by 9% (Rosenqvist) and 13% (Hess), based on the average difference between these and the subregional estimates for the seven locations with available data. If this holds true for the whole basin, the basin-scale maximum inundation would be around 10% higher.

3.1.2. Estimates based on SAR datasets

At the basin scale, SAR-based estimates of maximum annual inundation range from $424,600 \text{ km}^2$ (Rosenqvist) to $633,500 \text{ km}^2$ (Hess), and minimum inundation from $53,900 \text{ km}^2$ (Rosenqvist) to $284,200 \text{ km}^2$ (Hess), as shown in Fig. 5. By considering long-term maximum inundation (i.e., all pixels that were inundated at least once in the entire available time series), instead of annual maxima, the SAR-based estimates range from $506,400 \text{ km}^2$ (Chapman) to $659,100 \text{ km}^2$ (Rosenqvist) for the entire basin (Table 2). The minima vary from $42,400 \text{ km}^2$ (Rosenqvist) to $284,200 \text{ km}^2$ (Hess). This highlights the large differences that exist, especially for the minima, usually referred to as the “low-water period.” Chapman's dataset, based on the 2006–2011 ALOS

PALSAR archive, has a smaller total maximum inundation area than the other two SAR datasets, as well as a smaller estimate for minimum inundation in relation to Hess' estimate, which in turn was developed from SAR mosaics at two seasons spanning only one year (1995–1996). Differences among the three datasets may originate from differences in acquisition dates, interannual and seasonal inundation variability, algorithms, spatial resolutions, or inconsistencies regarding the data processing. For example, Chapman estimates long-term maxima and minima based on multiple years, while Hess and Rosenqvist provide annual values. The calibration uncertainty was also higher for the JERS-1 data used in Hess' mapping than in the subsequent satellites (ALOS-PALSAR and ALOS-2 PALSAR-2) (Hess et al., 2003). For long-term minimum inundation, the interannual variability seems to be a minor factor since the Hess dataset, which estimated a larger figure than the other ones, was developed for a year with minimum water levels higher than those during Chapman's acquisition dates, but lower than those during Rosenqvist's ones (see Fig. 8 in Rosenqvist et al., 2020). Thus, the larger minimum inundation extent by Hess et al. (2015) seems to be more related to algorithm differences (Fig. S2). For the maximum water levels, Hess' period was associated with an average year, below the water levels in Chapman and Rosenqvist, and this may explain the relatively higher long-term maximum inundation by Rosenqvist, while Chapman's smaller values are likely due to algorithm differences. For the western basin, Hess' estimate is based on JERS-1 data mostly from June 1996 (Hess et al., 2015), which likely missed some of the inundation in this region as in the Pacaya-Samiria region, and may partly explain the larger value by Rosenqvist (see section 3.2.2). Spatial resolution is also an important factor: Rosenqvist's resolution is 50 m, and it is capable of representing smaller floodplains than the other two (Fig. S3), as will be discussed in section 3.2.2.

3.1.3. Assessment of other datasets

The coarse-resolution datasets and hydrologic models generally estimate smaller annual maximum inundation areas in comparison to the SAR datasets, with the exception of SWAF-HR, WAD2M and CaMa-Flood that yield similar annual maximum inundation. This results from the low sensitivity of the passive microwave signal, which underlies most coarse-resolution datasets, to detect small fractional flooded areas within the grid cells, flooding under particularly dense vegetation, and flooding of short duration (i.e., less than one month of consecutive inundation) (Hamilton et al., 2002). The higher sensitivity of the SWAF-HR may be associated with the use of L-band passive microwave emission. Given the long-term data availability from dynamic, coarse-resolution datasets, their long-term mean estimates are closer to the SAR ones, varying from 450,800 km² (THMB) to 630,900 km² (SWAF-HR), when compared to the annual scale analysis. Therefore, no clear relationship between long-term minimum or maximum inundation and the spatial resolution of the datasets is observed (Fig. 6), which could be expected when analyzing the annual values (Fig. 5).

As expected, the optical-based datasets (GSWO, G3WBM, GLAD) cannot map inundation under dense vegetation canopies and thus lead to much lower estimates of basin-wide inundation area (Aires et al., 2018; Parrens et al., 2017). Similarly, ESA-CCI, which is based on land cover classification of optical imagery with the addition of SAR inputs for delineation of wetland areas, yields low basin-wide inundation areas, although relatively higher than the purely optical-based estimates. In contrast, the multi-satellite-based CIFOR provides an unrealistically large estimate of maximum inundation area (872,700 km²), which may be due to overestimation of soil moisture by the topographic index used. This method is sensitive to rainfall overestimation, which may have occurred in 2011, the year for which CIFOR was developed (Gumbrecht et al., 2017). While the dataset does represent well the spatial extent of peatlands across the Pacaya-Samiria region (Gumbrecht et al., 2017), its estimation of widespread inundation across the basin has limitations to represent the large Amazon river floodplains, especially the forested ones, which are classified as "swamps (including bogs)" by this dataset

together with extensive interfluvial areas (Fig. S4).

3.2. How much inundation is estimated to occur in individual wetland regions?

3.2.1. Overall assessment

The 18 basin-scale inundation datasets were compared with the 11 subregional ones through analysis of long-term means of annual maximum inundated areas (Table 3), long-term means of annual minimum areas (Supplementary Table S3), and multiple comparison metrics (Supplementary Table S4). The subregional datasets, covering individual wetland complexes, are considered as independent validation datasets, given the ground validation performed for most of them, as well as the use of a region-specific classification, and the often higher spatial resolution (e.g., 12.5 m for some based on ALOS-PALSAR imagery).

The Amazon River floodplains (from Iquitos to Gurupá) and the Llanos de Moxos regions are the largest Amazon wetland complexes: 106,800 ± 25,800 km² and 113,500 ± 53,400 km², respectively when considering the three SAR-based datasets, and 94,100 ± 32,500 km² and 85,300 ± 52,400 km² when considering all 18 basin-scale datasets. Besides these two areas, the third largest Amazon wetland region is Pacaya-Samiria, with 29,700 ± 20,600 km² (all datasets) and 40,000 ± 4200 km² (SAR datasets).

The comparison of the long-term means of annual maximum and minimum observed inundation over the available time periods indicates differences between basin-scale datasets and the subregional validation datasets. Overall, the subregional datasets had a larger maximum inundation extent than that estimated for the subregion from the basin-scale datasets. The underestimation by the basin-scale ones varied from 49% for the Pacaya-Samiria region to 5% for the lower Amazon River floodplain. Only three datasets overestimated the maximum extent of inundation: GIEMS-D3, GIEMS-D15 and GLWD. The basin-scale, SAR-based ones (Hess, Chapman and Rosenqvist) underestimated the maximum extent in the regions represented by all subregional datasets, except Rosenqvist for Janauacá Lake, and Hess for the Llanos de Moxos region. This is likely related to the higher resolution of many of the subregional datasets (e.g., 12.5 m original and 25 m final resolution for the Uatumá ALOS-PALSAR classification by de Resende et al., 2019), differences in image acquisition period, and fine-tuning that may occur with dedicated processing for a particular region.

To investigate the depiction of seasonal patterns of inundation by the various datasets, we assessed the correlation between the time series of absolute inundated areas from the dynamic ones and the estimates for individual wetland complexes (Table S3). Overall, all datasets agreed well (average Pearson correlation larger than 0.63 for the four wetland complexes with available time series), showing a similar depiction of the inundation seasonality. However, their ability to monitor high-resolution flood frequency is limited, as will be further discussed in section 4. A visual comparison of the time series (Fig. S6) shows agreement on seasonal timing of flooding and drainage, but disagreement in the extent of inundation. In particular, two datasets have a small overall annual amplitude (SWAMPS and WAD2M).

Overall, four datasets had the best overall representation of spatial patterns in inundation (Fit metric; see Eq. (1)), as analyzed at 1 km pixel resolution, in comparison to the subregional validation datasets: Hess, GLWD and the two hydrodynamic models (MGB and CaMa-Flood), which were associated with average Fit metric between 0.64 and 0.67 (Table S3). While hydrologic models such as MGB, CaMa-Flood and THMB have a satisfactory agreement basin wide, they are unable to represent wetlands not primarily inundated by rivers (Fleischmann et al., 2020; Zhou et al., 2021). For example, the Llanos de Moxos inundation is underestimated by both CaMa-Flood and MGB with low Fit metric values (0.19–0.28; Table S3). This is expected for interfluvial wetlands such as Llanos de Moxos and Roraima, where much of the flooding is caused by poor drainage of local rainfall and tends to be shallower, as opposed to overflow of large rivers onto adjacent

Table 3

Long-term maximum inundation areas (km^2) for the 11 wetland complexes (up to three subregional datasets per complex) and the 18 basin-scale datasets. The subregional values refer to the following datasets, in this order (semicolon-separated values relate to areas with more than one dataset available): Curuai - ALOS (Arnesen et al., 2013) and LISFLOOD-FP model (Rudorff et al., 2014); Uatumá - ALOS (de Resende et al., 2019); Janauacá - ALOS (Pinel et al., 2019), hydrologic model (Bonnet et al., 2017) and TELEMAC-2D model (Pinel et al., 2019); Mamirauá - ALOS (Ferreira-Ferreira et al., 2015); Pacaya-Samiria - ALOS-2 PALSAR-2 (Jensen et al., 2018); Llanos de Moxos - MODIS (Ovando et al., 2016) and ALOS (Ovando et al., 2016); and Lower Amazon River - MODIS (Park and Latrubesse, 2019). Average, standard deviation (S.D.) and coefficient of variation (CV) are presented for each area in the last rows.

	Dataset	Curuai	Uatumá	Janauacá	Mamirauá	Pacaya-Samiria	Llanos de Moxos	Lower Amazon	Amazon mainstem	Purus	Roraima savannas	Negro campinas and campinaranas
	Subregional	4162; 3720	1471	404; 336; 176	4476	57,913	125,422; 133,470	56,722	–	–	–	–
Multiple datasets at coarse resolution	GIEMS-2	3080	984	623	3344	23,344	156,176	79,871	116,379	7208	7173	12,237
	SWAMPS	3359	722	280	1131	9929	88,753	58,626	72,468	5618	4970	8819
	WAD2M	681	243	166	888	42,635	102,780	29,276	49,261	6698	3173	15,450
Multiple datasets at high resolution	GIEMS-D3	4643	2732	505	3569	11,562	150,285	92,908	127,552	9045	12,355	15,123
	CIFOR	3796	994	177	1714	52,590	116,201	43,509	86,301	10,844	3728	20,712
	ESA-CCI	3236	855	260	3045	28,727	39,795	37,475	84,803	8883	510	12,623
Hydrological model	GIEMS-D15	4635	2681	416	2444	44,536	117,979	86,123	127,150	11,186	8129	14,854
	GLWD	4275	2267	535	4259	79,124	40,661	67,746	140,921	14,840	1048	95
	SWAF-HR	4439	2199	388	3205	16,900	159,712	69,539	110,468	10,785	18,146	15,375
Optical sensors	THMB	2883	554	164	2840	27,748	52,693	39,193	89,658	19,733	4307	3640
	CaMa-Flood	4246	1613	534	3208	34,096	80,725	63,963	118,577	20,947	3454	6560
	MGB	4098	1549	474	3750	33,344	21,757	61,997	115,047	20,394	240	3224
Synthetic Aperture Radar	G3WBM	2732	628	135	795	2694	9564	27,451	37,718	2351	352	1238
	GLAD	3479	832	204	1141	4196	38,897	36,930	53,121	3903	3495	3885
	GSWO	3163	675	150	962	3637	19,240	31,191	44,731	2982	1442	1880
	Chapman	2796	934	184	2694	24,001	73,710	39,677	77,632	12,499	4077	5935
	Hess	3996	1045	209	3985	39,741	174,198	52,156	115,822	15,155	8950	15,758
	Rosenqvist	3055	1238	446	4362	56,160	92,693	55,262	126,806	20,738	1867	9935
	Average	3477	1264	325	2630	29,720	85,323	54,050	94,134	11,323	4856	9297
	S.D.	949	748	163	1226	20,591	52,387	19,956	32,503	6185	4666	6201
	CV	27%	59%	50%	47%	69%	61%	37%	35%	55%	96%	67%

floodplains. The four alternative subregional datasets assessed here - three hydrological models (one for Curuai and two for Janauacá) and one classification of ALOS-PALSAR data for the Llanos de Moxos area - were generally better or similar to some of the best-performing basin-scale ones, as could be expected given their fine tuning for the specific areas, which often includes local topographic surveys.

Some of the datasets merging multiple data sources overestimated the inundation area of individual wetland complexes the most, especially GIEMS-D15, GIEMS-D3 and GLWD. Furthermore, CIFOR was originally designed for peatland mapping in the tropics, and generally overestimates inundation, suggesting a widespread distribution of wetlands along interfluvial terraces across the whole basin that may include areas of poorly drained soils lacking surface water. For the individual wetland complexes, however, CIFOR generally underestimated inundation and had a poor representation of spatial patterns of inundation (low Fit metric). WAD2M underestimated the maximum inundation the most, which is understandable given its removal of open water areas and because its main inputs (CIFOR and SWAMPS) also underestimated inundated areas as indicated by the subregional validation datasets.

3.2.2. Individual inundation patterns based on SAR data

Regarding the maximum inundation extent, the Janauacá case provides a representative example to understand the differences among multiple L-band SAR datasets: these estimated total inundated area as 209 km^2 , 184 km^2 and 446 km^2 for Hess, Chapman and Rosenqvist, respectively, in contrast to 404 km^2 with the subregional ALOS-PALSAR-based dataset (12.5 m resolution; Pinel et al., 2019). Part of these differences occur because of interannual variability, but other factors such as spatial resolution and algorithm differences seem relevant. Rosenqvist led to a more consistent estimation of the spatial inundation extent in terms of maximum inundation (Table 3) and inundation spatial patterns (Fit metric; Table S3), which can be a consequence of its higher spatial resolution (50 m) in contrast to the other two (90 m; Fig. S3).

Overall, Rosenqvist provided the largest inundation extent among SAR datasets across all areas along the Amazon mainstem floodplain, except for the Curuai floodplain and the savanna wetlands, as well as the closest agreement with subregional validation datasets ($-9\% \pm 13\%$; average \pm S.D.). Hess estimated the largest inundation area in the wetlands associated with savannas (Llanos de Moxos and Roraima) and campinas and campinaranas (Negro). However, Hess' estimate is 39% larger than the subregional validation dataset for Llanos de Moxos, while the other two SAR estimates are lower (-26% and -41% for Chapman and Rosenqvist, respectively).

One important question remains about the low-water period, as discussed in the previous section for the basin-scale analysis. Hess suggests much more inundation for this period for the Amazon mainstem floodplains ($54,500 \text{ km}^2$), mainly for the upstream forested reaches, and for the whole basin in general ($284,200 \text{ km}^2$), than recent estimates with ALOS ($28,500$ and $91,200 \text{ km}^2$) and ALOS-2 data ($19,500$ and $42,400 \text{ km}^2$). An assessment with the subregional datasets along the Amazon floodplain suggests that Hess overestimates the minimum extent for Curuai, Mamirauá and lower Amazon River, and is accurate for the Janauacá floodplain lake. Rosenqvist generally underestimates the minimum inundation. For instance, for the Mamirauá dataset, the minimum extent (i.e., permanently flooded areas) sums up to 715 km^2 , which is increased to 1545 km^2 if considering all pixels flooded for more than 295 days per year. For this area, the SAR estimates are 1756 km^2 (Hess), 866 km^2 (Chapman) and 422 km^2 (Rosenqvist). Overall, this suggests that the actual value of minimum inundation across the central Amazon floodplains is somewhere between the Hess and Rosenqvist estimates.

3.2.3. Challenges over floodable savannas, campinas and campinaranas

Large discrepancies are observed for the Roraima and Negro wetlands. Roraima wetlands are small river floodplains interspersed with open savannas subject to flooding, which can be identified by optical

data. In addition, the typical timing of high and low water in the Roraima region coincides approximately with the JERS-1 dual-season mosaics that were designed to reflect the seasonality of the central Amazon River floodplain (Hamilton et al., 2002). For these reasons, the JERS-1-based dataset by Hess et al. (2015) seems to satisfactorily represent most of the Roraima wetlands. However, it misses some small-scale riparian forests, given its 90 m spatial resolution and snapshot coverage that likely missed flooding events on smaller, flashier rivers (Fig. S5). Thus, the maximum inundation is likely higher than the Hess estimate (8900 km²), which in turn is larger than the other ones based on SAR (1900–4100 km²). The only dataset to estimate a higher value is the coarse SWAF-HR (18,100 km²), which is similar to the value previously estimated by Hamilton et al. (2002) (16,500 km²), also with coarse data (SMMR passive microwave), though a part of the discrepancy may be due to interannual variability. More studies are necessary for this area to understand its actual inundation extent and dynamics. Similarly, the inundation estimates in the Negro interfluvial areas are subject to large uncertainty, with the long-term maximum inundation varying between 95 (GLWD) and 20,700 km² (CIFOR), considering all basin-scale datasets. SAR-based estimates were between 5900 and 15,800 km². In contrast, for the Pacaya-Samiria interfluvial area, which includes a large complex of forested wetlands, peatlands and palm swamps, the discrepancies are smaller than for the other interfluvial regions, although still considerable. The basin-scale SAR ranged between 24,000 km² (Chapman) and 56,200 km² (Rosenqvist), with the subregional

validation dataset yielding 57,900 km². The good agreement between Rosenqvist and the subregional dataset was already reported by Rosenqvist et al. (2020).

3.3. How much do the datasets agree on the spatial distribution of inundation?

Agreement maps of the high resolution datasets (≤ 1 km spatial resolution) were developed for both long-term maximum (14 datasets available) and minimum inundation areas (10 datasets), based on the number of inundation datasets coinciding over a 1 km pixel (Figs. 7 and 8 and their categorization for specific regions in Fig. 9). Overall, 31% of the Amazon lowlands area (i.e., 1.59×10^6 km² out of 5.11×10^6 km²) has been estimated as subject to inundation by at least one dataset (bottom left panel, Fig. 7). Based on the agreement between two datasets, this value decreases to 948,300 km², which is larger than the value estimated when there is agreement among four datasets (553,200 km²). This latter estimate is more similar to the average maximum inundation as estimated by the ensemble of datasets (559,300 km²) and the three SAR-based ones (599,700 km²). Furthermore, there is a lower agreement for the minimum inundation than for the maximum inundation among individual regions (Fig. 9).

For specific regions, a high degree of agreement for floodplains dominated by open water areas is evident for the lower Amazon River reaches, followed by the forested floodplains fringing large rivers,

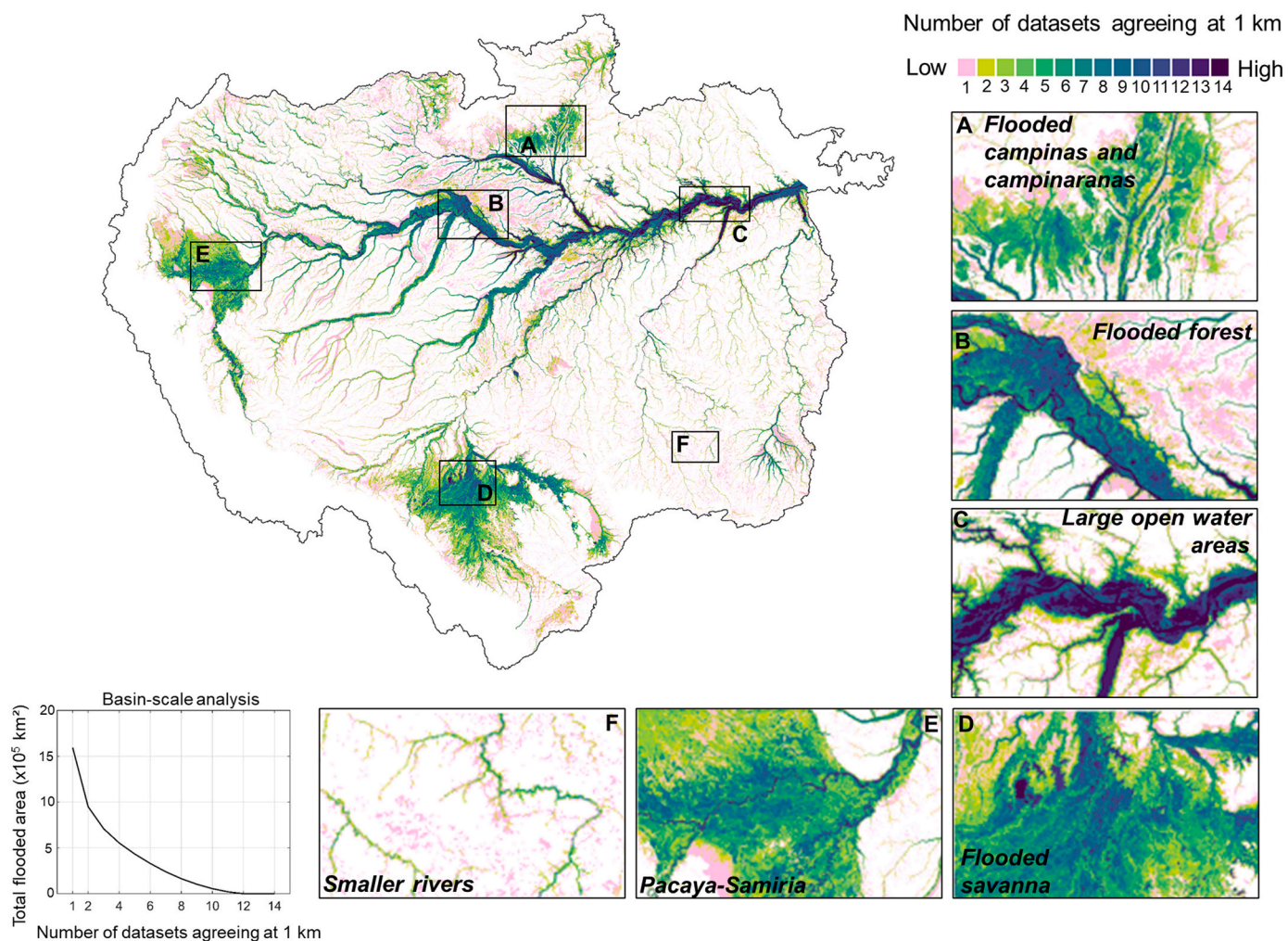


Fig. 7. Agreement for maximum inundation area among 14 basin-scale datasets at high resolution (≤ 1 km spatial resolution): G3WBM, ESA-CCI, GLAD, GSWO, GLWD, CIFOR, GIEMS-D15, GIEMS-D3, Chapman, Hess, Rosenqvist, SWAF-HR, CaMa-Flood and MGB. A given pixel of a dataset with resolution higher than 1 km that had more than 50% of flooding at the maximum inundation extent is classified as inundated.

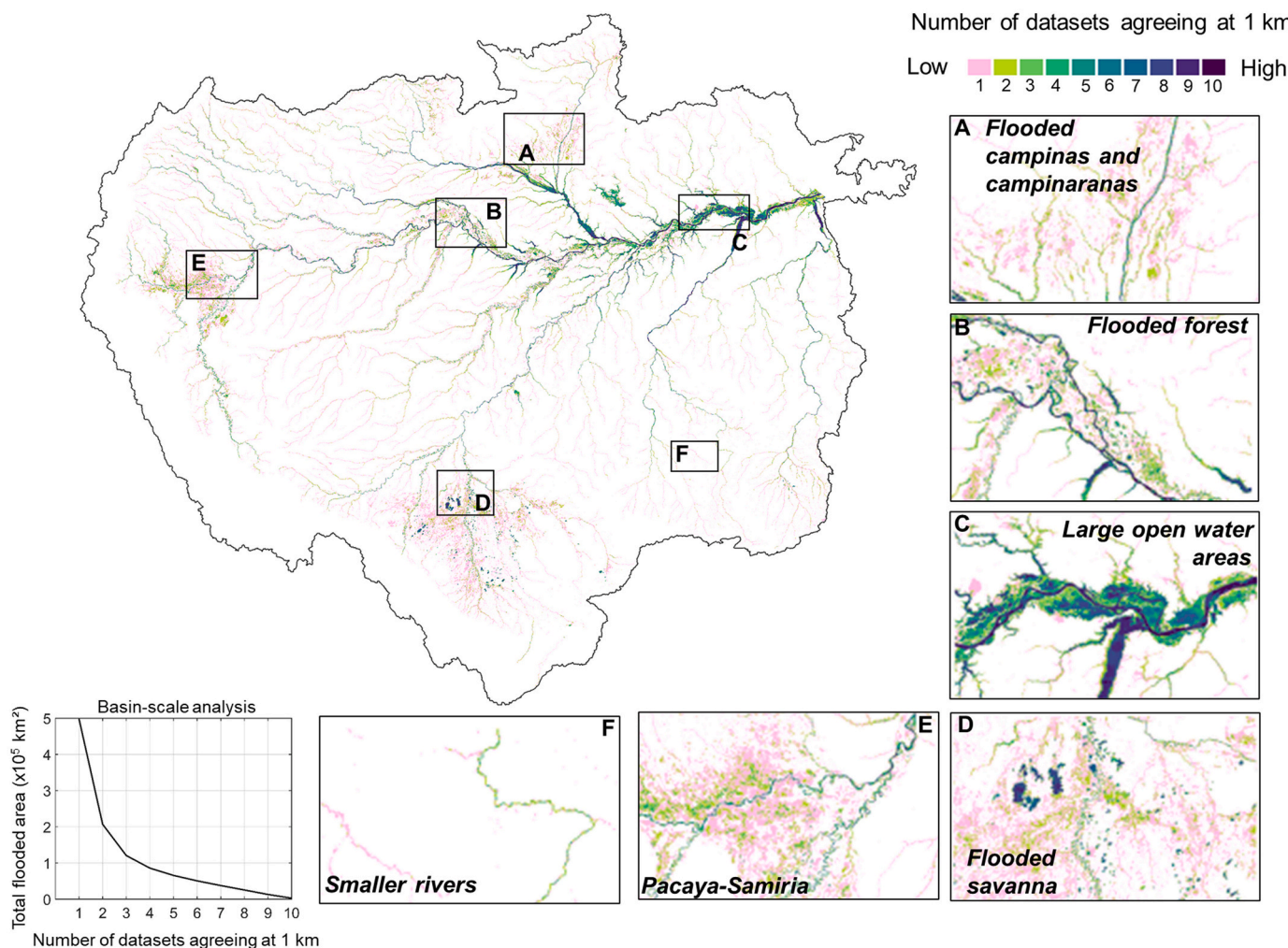


Fig. 8. Agreement for minimum inundation area among 10 basin-scale datasets at high resolution (≤ 1 km spatial resolution): GIEMS-D15, Chapman, Hess, Rosenqvist, SWAF-HR, CaMa-Flood, MGB, GIEMS-D3, GSWO and GLAD. A given pixel of a dataset with resolution higher than 1 km that had more than 50% of flooding at the minimum inundation extent is classified as inundated.

especially along the Amazon mainstem, Purus and Negro rivers. The generally higher accuracies over central Amazon floodplains may also be related to the attention that dataset developers have devoted to it, in contrast to other regions. Furthermore, the maximum floodplain extent can be somewhat delineated with terrain elevation data (i.e., DEMs) using algorithms such as HAND (Rennó et al., 2008), which helps to explain the relatively small disagreement for floodplains fringing the largest rivers, and is particularly effective with vegetation bias-removed DEMs (O'Loughlin et al., 2016; Yamazaki et al., 2017). The best agreement (for both maximum and minimum inundation extent) occurred over the Curuáí floodplain along the lower Amazon mainstem, with 37% of its area being estimated as subject to inundation by all 14 datasets (Fig. 9a). An agreement among all 14 datasets occurred, in part (i.e., more than 10% of the wetland area), for the central Amazon floodplains (Curuáí, Uatumá, Janauacá and lower Amazon River) because of their relatively large fractions of open water areas.

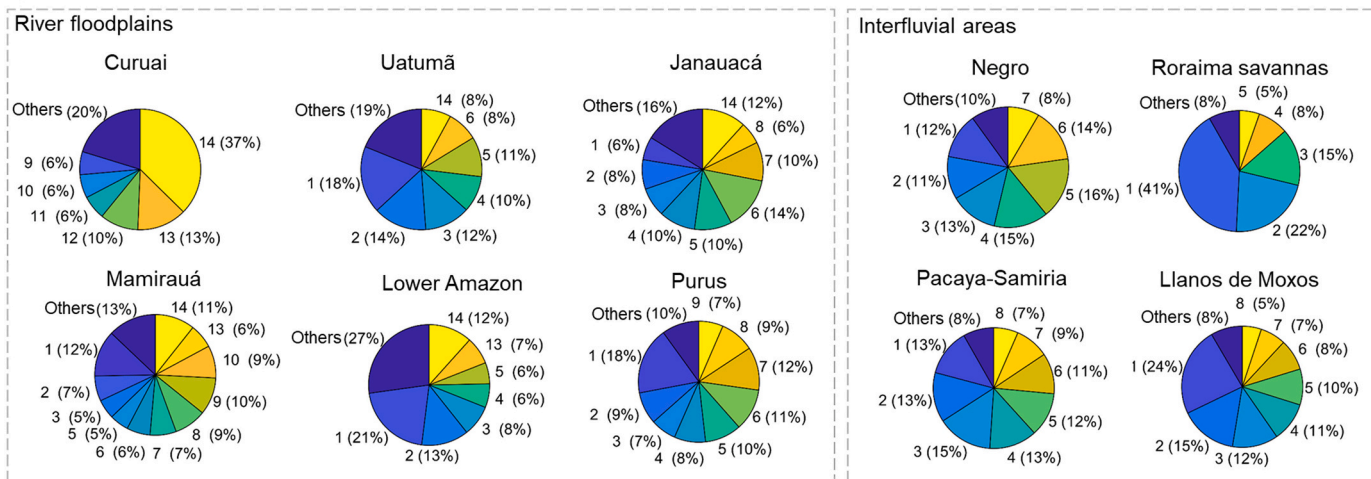
In the interfluvial wetlands (Negro campinas and campinaranas, Roraima savannas, Pacaya-Samiria and Llanos de Moxos), the inundation patterns are less dependent on riverine overflow and more dependent on local rainfall, making them less predictable (Hess et al., 2003). The disagreement for both maximum and minimum inundation area is the largest across all regions, e.g., 65–78% of their flooded areas were mapped by only one model for the minimum inundation (Fig. 9b). The Llanos de Moxos is conspicuous as a region of particular disagreement,

perhaps because flooding is mainly shallow and in vegetated areas (mainly savannas/grasslands), and is highly variable from year to year. In general, the smaller the flooded patches the higher the challenge to map them, not only because of resolution but also due to small-scale variation in topography. Similar disagreement occurred in other interfluvial wetlands such as the Negro and Roraima ones, and would be expected elsewhere in savanna wetlands of South America (e.g., Pantanal, Llanos de Orinoco and Bananal Island; Hamilton et al., 2002). The poor agreement over interfluvial areas, however, may also partly reflect the longer history of study of Amazon mainstem floodplains, for which there are river gage records that reflect floodplain water levels and inundation, while more remote areas such as the Negro interfluvial areas and Pacaya-Samiria regions are more challenging to represent with a few gages, and have received less attention. The challenges in estimating inundation over interfluvial areas also affect the SAR-based datasets, which disagreed the most over these regions (see section 3.5 and discussion in Rosenqvist et al., 2020).

3.4. Quantifying the inundation extent of different wetland types

Amazon wetlands include a myriad of ecosystems varying in geomorphology, hydrology, and vegetation cover. The classification system proposed by Junk et al. (2011) differentiated Amazon wetlands according to amplitude of water level. Wetland types ranged from the

a) Maximum inundation



b) Minimum inundation

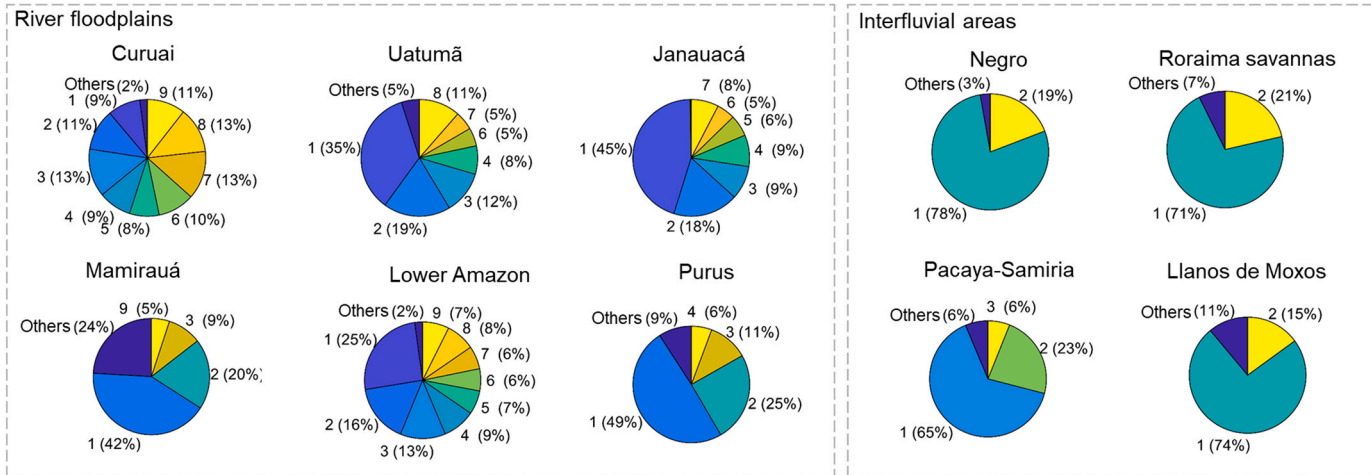


Fig. 9. Degree of agreement for (a) maximum and (b) minimum inundation area for 10 individual wetland complexes, based on the 1 km agreement map (Figs. 7 and 8). The percentage values indicate the fraction of each area where a given number of datasets agreed that it was flooded, e.g., 14 models agreed that 37% of the Curuai area was flooded in the maximum inundation extent. The class with number 1 indicates the fraction of the area that only one dataset estimated as being inundated. The class “others” refers to all classes that had less than 5% of pixels estimated as being inundated.

forested swamps with stable water levels to river floodplains with oscillating water levels, and to interfluvial areas with small seasonal water level amplitude due to the main contribution of local rainfall and runoff (Fleischmann et al., 2020; Junk et al., 2011; Ovando et al., 2018).

A simpler yet hydrologically meaningful classification is the categorization into river floodplains and interfluvial wetlands adopted here, since the former typically have a greater hydrological connection to the main river and thus are subject to a different control of inundation area by river levels (Reis et al., 2019). We performed a quantitative analysis of the inundation area in these two main hydrological classes. All pixels considered flooded by at least two datasets, based on the 1 km agreement map for maximum inundation extent (Fig. 7), are presented in Fig. 10. Overall, the medium to large river floodplains (upstream drainage area $> 1000 \text{ km}^2$) have a larger inundation extent than the category with small floodplains and interfluvial areas. An average total area subject to inundation of $317,800 \pm 84,400 \text{ km}^2$ (average \pm S.D.; median equal to $323,700 \text{ km}^2$) was obtained for the medium to large floodplains, not including the optical and land cover datasets (G3WBM, GLAD, GSWO and ESA-CCI). A greater area for large floodplains was estimated by all except for CIFOR, SWAMPS and WAD2M. Two datasets estimated a similar value between the two classes (Chapman and GIEMS-2), which may be related to an overestimation of basin-scale

isolated flooded patches.

Large floodplains fringing the main rivers, especially along the Amazon River, have been largely addressed by previous studies (Table 1 and Table S1). However, large river floodplains are also present in less studied reaches, e.g., in the upper Napo and Içá rivers in northwest Amazon basin, and upper Xingu in the southeastern portion (see location in Fig. 1). These upper reaches are subject to more sporadic, flashy river hydrological regimes (Hamilton et al., 2007), which make their inundation area difficult to map with current datasets of relatively low temporal resolution. In our analysis, the non-floodplain areas include mainly the large interfluvial areas (black rectangles in Fig. 10), small river floodplains that are challenging to detect with currently available datasets, and some reservoirs, such as Balbina reservoir on the Uatumã River.

Besides the central Amazon floodplains, which have been widely studied, other wetland complexes require more attention, such as the Negro and Roraima interfluvial areas; the latter was only assessed by a single study to our knowledge (Hamilton et al., 2002). The inundation mapping of the Pacaya-Samiria region in the upper Amazon has received scientific attention recently (Jensen et al., 2018; Rodriguez-Alvarez et al., 2019), partially because of the region's role as a carbon sink via formation of peat (Draper et al., 2014; Lähteenoja et al., 2012).

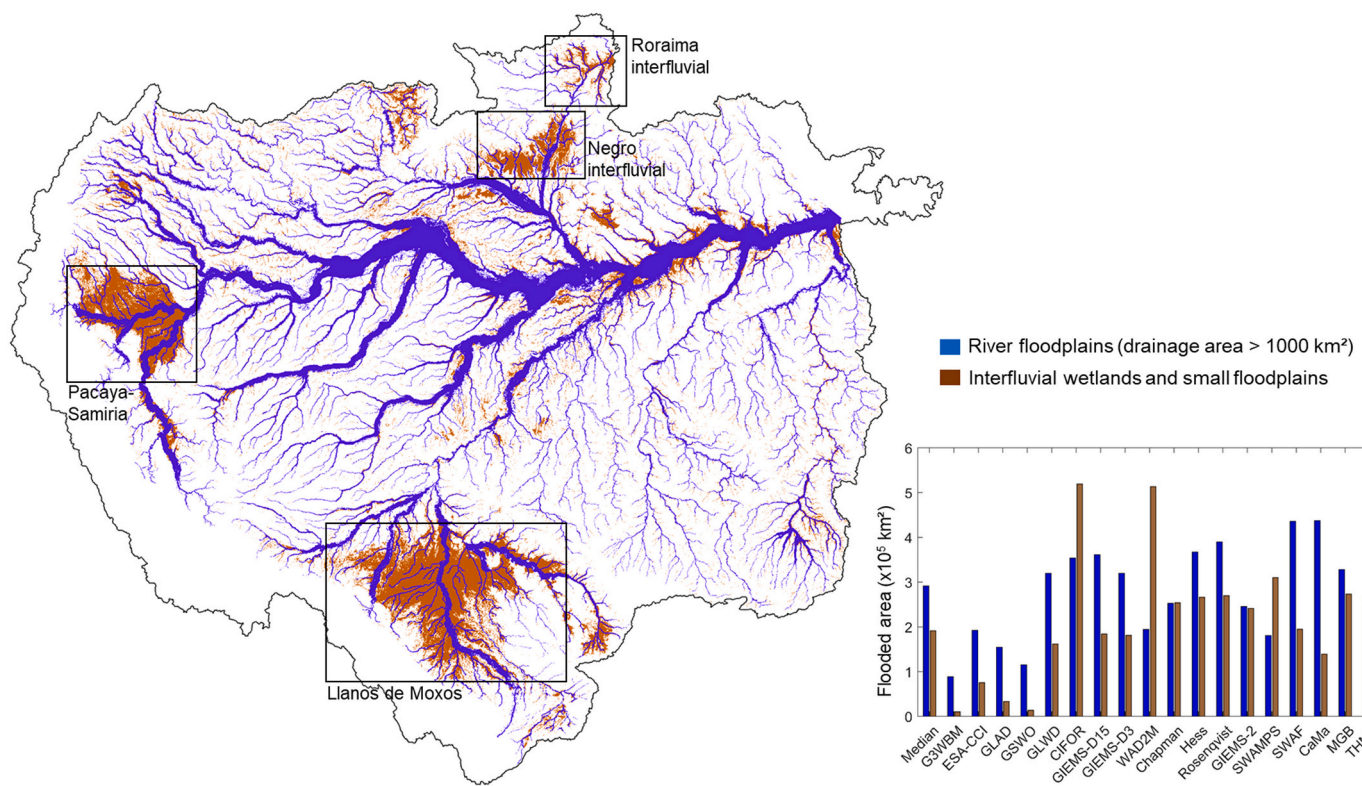


Fig. 10. Quantification of maximum inundated areas over river floodplains with drainage area larger than 1000 km², and interfluvial wetlands and small floodplains (area < 1000 km²) within the Amazon basin. The maximum inundation map depicts all 1 km pixels with at least two datasets agreeing (i.e., a reclassification of Fig. 7), in order to avoid overestimation caused by pixels with only one dataset classifying them as subject to inundation. The four large areas of interfluvial wetlands are highlighted with black rectangles (Pacaya-Samiria, Llanos de Moxos, Negro campinanas, and campinaranas, and Roraima savannas).

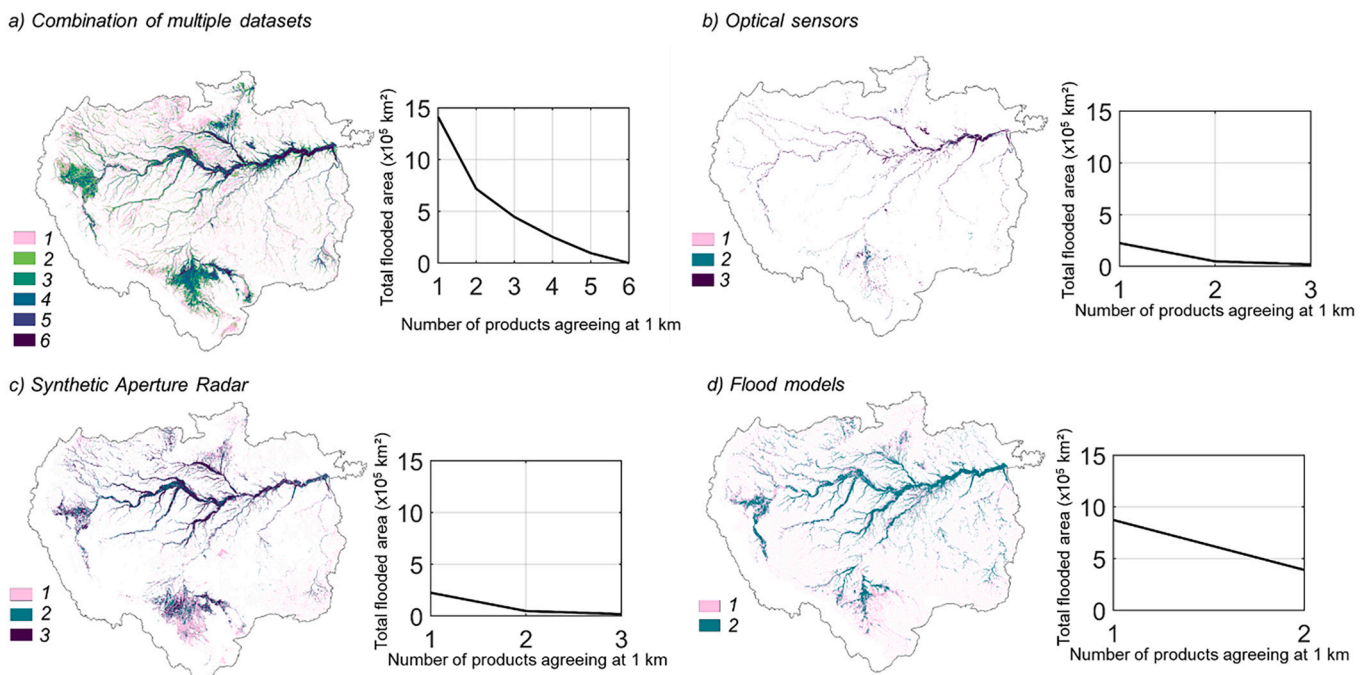


Fig. 11. Amazon basin (< 500 m elevation) agreement maps at 1 km resolution, for maximum inundation and for each type of dataset, considering only the high-resolution datasets (≤ 1 km spatial resolution): (a) six datasets based on merging of multiple datasets (GLWD, CIFOR, GIEMS-D3, GIEMS-D15, SWAF-HR, ESA-CCI), (b) three datasets based on optical sensors (G3WBM, GLAD, GSWO), (c) three datasets based on synthetic aperture radar (Hess, Chapman, Rosengqvist), and (d) two hydrological models (MGB and CaMa-Flood). The right column graphs present the total inundation area in the Amazon basin for a given number of datasets agreeing, e.g., the basin area where the two hydrological models (Fig. d) agree to be flooded is 390,900 km².

Regarding open water areas, Melack (2016) reported values ranging from 64,800 km² (Melack and Hess, 2010) to 72,000 km² (SRTM Water Body Data) and 92,000 km² (Hansen et al., 2013) for the Amazon basin (< 500 m in elevation). The three Landsat-based datasets assessed here, which are mainly capable of detecting open water areas, estimate 98,500 km² (G3WBM), 128,500 km (GSWO) and 187,600 km² (GLAD).

3.5. Limitations in comparing the inundation area datasets

Some of the differences in large-scale inundation mapping highlighted by our comparison occur because distinct datasets map temporal variation in inundation in different ways, varying for example in sensor type, post processing, and spatial resolution. Fig. 11 shows the agreement maps for maximum inundation for four classes of datasets, considering the 14 basin-scale high-resolution datasets. Those based on multiple datasets (GLWD, CIFOR, GIEMS-D3, GIEMS-D15, SWAF-HR) have the best agreement for the Llanos de Moxos area, and to a smaller degree, for Pacaya-Samiria, Negro and Roraima wetlands. The L-band SAR datasets have less overall agreement (Fig. 11c), while the optical data are mainly applicable to open water areas in the Amazon mainstem floodplain (Fig. 11b). The 1D hydrological models cannot represent interfluvial wetlands where flooding is not controlled by river level and discharge (Fig. 11d).

The different methodologies used to produce each dataset complicate their direct comparison (Rosenqvist et al., 2020), and some methodological differences produce systematic differences and bias among the data sources included in our comparison. Here we used datasets covering long-term dynamics (e.g., GIEMS or hydrologic models), short-term dual-season (e.g., Rosenqvist, spanning four years), and a particular year (e.g., Hess). Some datasets use alternative approaches to derive long-term maximum inundation area, such as GIEMS-D15, which generated estimates by merging 3-year moving-window maximum values of GIEMS with the GLWD dataset. Therefore, a comparison of all these datasets must be performed with consideration of their methodology. For instance, the comparison of dual-season datasets against monthly datasets can yield erroneous conclusions, although it has been a common practice to directly compare such datasets. Some datasets also consider a “high-water assumption” (Ferreira-Ferreira et al., 2015; Hess et al., 2003), whereby the high-water maps are forced to contain all flooded pixels from the low-water map.

In addition to methodological differences, each dataset was developed for different periods (Table 1), and thus interannual and seasonal variability accounts for some of the differences among them. To address this, we performed an annual analysis (Fig. 5), which suggests that the long-term inundation estimate is fairly stable for each dataset despite some interannual differences. In fact, the temporal variability of each dataset is generally smaller than the differences in comparison with the other estimates. However, the Amazon hydrological cycle has been shifting over decades (Barichivich et al., 2018; Gloor et al., 2013), and a recent increase in maximum water levels in the central Amazon suggests a new hydroclimatic state (Espinoza Villar et al., 2019). Some wetlands have also been subject to forest loss, and so the detectability of inundation by remote sensing may have increased over time, e.g., major deforestation has occurred along the lower Amazon River floodplain (Renó et al., 2011). Similarly, widespread burning might be converting black-water floodplain forests into savanna vegetation (Flores and Holmgren, 2021). In addition, in some regions, such as the southern Amazon, an increase in the dry-season length has been observed, which is a major climatic constraint for forest sustainability (Fu et al., 2013; Staver et al., 2011). However, analyzing long-term change in inundation patterns is beyond the scope of this study, and thus we assumed stationarity in our comparison framework.

Another important challenge is to find a common definition of wetlands among datasets. Here we focused on inundation extent, however some datasets (e.g., CIFOR) represent peatland locations instead of inundated areas, although their areas of peat formation often include

inundated areas. Estimates based on SAR or passive microwave emission may also be sensitive to saturated soil without standing water above it, and thus the observed inundation estimates can have some ambiguity. Hydrologic models provide simulated surface water extent, and we mapped inundation accounting for pixels with water depth greater than zero. While hydrologic models have uncertainties related to model structure (e.g., inadequate representation of inundation processes), input data (e.g., DEM and climate forcing) and parameterization (e.g., soil water capacity and river channel width and depth; assumptions of level water surfaces between rivers and their floodplains), remote sensing-based datasets have uncertainties related to spatial and temporal resolutions (e.g., coarse spatial resolution not capable of detecting small patches), and detection uncertainty (e.g., dense vegetation canopies can obscure passive microwave emission from underlying surfaces). Thus, a comparative framework provides an opportunity to highlight and stress the uncertainties and limitations of each dataset.

Hydrologic models currently available at the Amazon basin scale are one-dimensional, and thus are capable of simulating flooding mainly along river floodplains, as corroborated by various validation exercises in the Amazon that have relied on the Hess, GIEMS and SWAF-HR datasets (Fleischmann et al., 2020; Luo et al., 2017; Paiva et al., 2013; Zhou et al., 2021). These models are also largely dependent upon accurate DEMs, which are still challenging to obtain over tropical forested floodplains. Furthermore, given that a 500 m elevation mask (Amazon lowlands) has been used for some SAR datasets (Hess et al., 2015), and the difficulty of some radar and passive microwave ones to detect inundation at high elevations due to slope and snow effects, for instance (Parrens et al., 2017), we have adopted the same 500 m threshold in our lowland mask to improve the comparability among datasets. However, even though higher elevation wetlands amount to much less total area compared to lowland wetlands, understanding their flooding dynamics is important for some parts of the Amazon basin. Although some datasets, especially the hydrological models (MGB, CaMa-Flood and THMB), are capable of estimating inundation in higher elevation parts of the basin, in this case uncertainties may also be large given errors in precipitation (low density of in situ gauges and high rainfall spatial heterogeneity) and thus runoff fields over mountainous areas, as well as the tendency for river flows to vary over short time scales (Espinoza Villar et al., 2009; Zubieta et al., 2015). Furthermore, the availability of in situ river discharge measurements for model calibration and validation is lower in the Andean Amazon (Feng et al., 2020; Wongchuig et al., 2019; Zubieta et al., 2017).

Our analyses were performed at 1 km resolution and at regional scales, which avoids geolocation problems that affect analyses at higher resolutions (e.g., 30 or 90 m). Small disagreements among our estimates and the values presented in the original publications may also arise from the use of the WGS84 datum with a geographical coordinate system for all datasets (except for SWAMPS which was provided in the EASE-Grid format). Also, the coarse-resolution datasets, especially GIEMS-2 and SWAMPS with 25 km spatial resolution, can be difficult to compare with estimates for individual wetland complexes (e.g., Curuai and Janauacá), since only a few 25-km pixels may be located within the wetland boundaries.

The quantification of inundation over larger river floodplains (Fig. 10) is also subject to uncertainties. The maximum floodplain lateral extent was estimated based on an automatic buffer procedure around the Hydrosheds drainage network, further manually edited by considering the three SAR-based, basin-scale datasets and the MERIT DEM-based topography. Although it captures the basin-scale geomorphological differences along major floodplains, some uncertainties remain regarding the true lateral extent for areas where rain-fed savanna wetlands are present (e.g., Llanos de Moxos, Roraima), and where inundation extends far from the main rivers (e.g., Pacaya-Samiria). For these areas in particular, we assumed buffer values similar to adjacent upstream and downstream floodplains (e.g., the Amazon River downstream of Pacaya-Samiria), which is reasonable but should undergo

future scrutiny, including local ground-based surveys.

4. Perspectives and recommendations

Considerable advances have been achieved in recent decades in the mapping of inundation extent across the Amazon basin. Here, we have presented an analysis of 29 inundation datasets for the basin, covering multiple scales, spatial and temporal resolutions, and data sources. We showed that large discrepancies persist, and this is especially true at local scales. Below we present some perspectives and recommendations

for future development of inundation mapping in the world's largest river basin.

4.1. Which are the most reliable data sources for inundation mapping in the Amazon River basin?

At basin scale, the Rosenqvist ALOS-2 PALSAR-2 dataset is available at 50 m, and shows a good overall agreement with the 90 m Hess one over the large river floodplains, while the latter seems more accurate for interfluvial wetlands (e.g., Negro and Roraima). The high agreement is

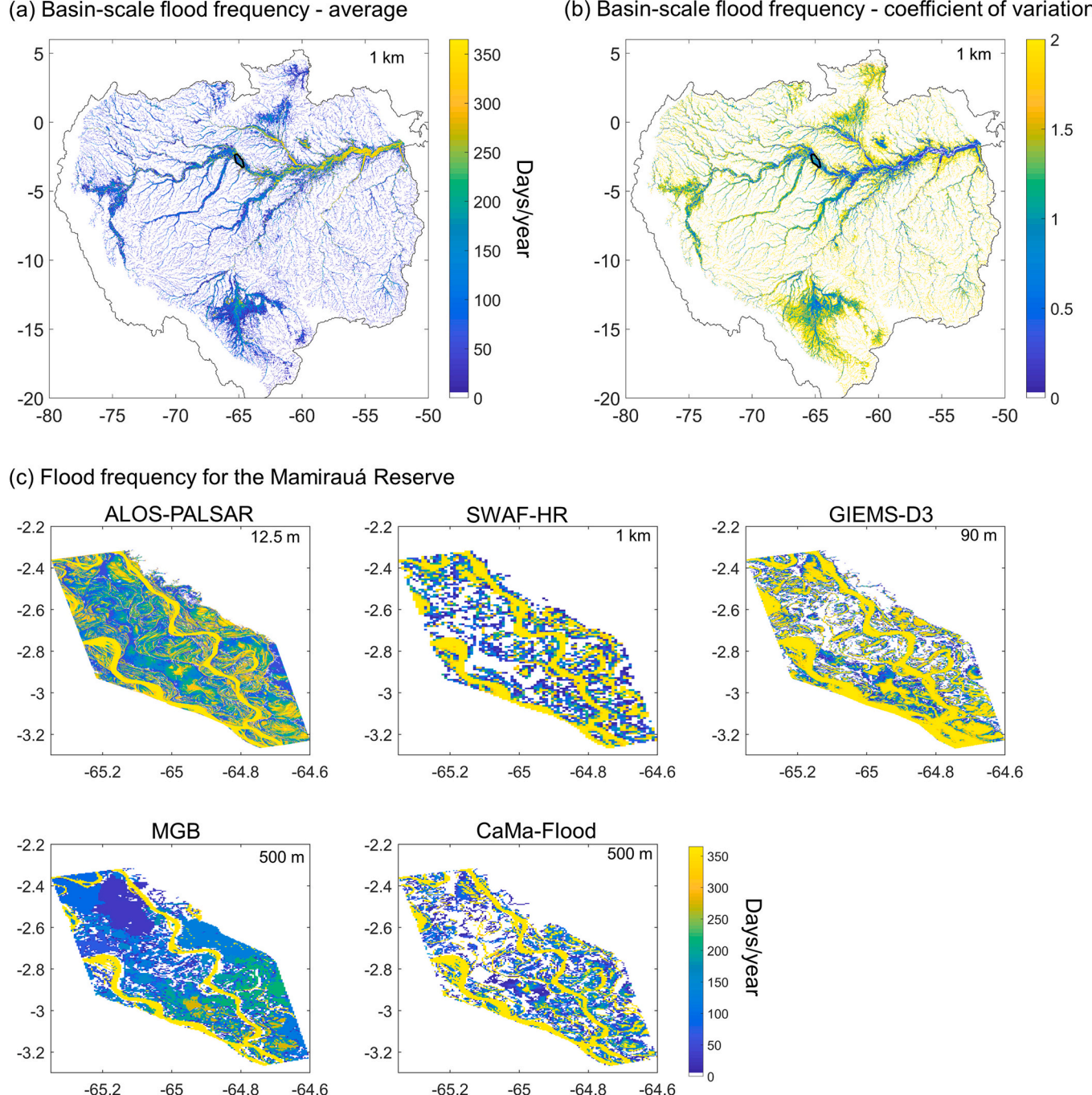


Fig. 12. Analysis of flood frequency for (a) basin-scale average and (b) coefficient of variation of the long-term flood frequency estimated from four high-resolution dynamic datasets (GIEMS-D3, SWAF-HR, CaMa-Flood and MGB). (c) The four basin-scale datasets are compared to a subregional validation dataset (i.e., the ALOS-PALSAR-based classification by Ferreira-Ferreira et al. (2015), displayed in the top left panel) for the Mamirauá Sustainable Development Reserve along the central Amazon River mainstem (location shown by black outline in figure a).

observed mainly for the maximum inundation estimates, while for the minimum inundation area, important disagreements persist and more studies should be performed to understand them. Overall, the Hess' dataset has been the Amazon inundation benchmark for many years, and still provides satisfactory estimates. Detection of inundation by L-band SAR has a sound theoretical and empirical basis that has been validated for the Amazon (Rosenqvist et al., 2002; Hess et al., 2003). Optical datasets with resolution higher than 30 m are available, but detection of inundation is restricted to non-vegetated wetlands and clear-sky periods, and is most applicable in the lower Amazon River floodplains. ALOS-PALSAR at 12.5 m resolution and Sentinel SAR at 10 m resolution (with C-band and limited vegetation penetration) can be applied to specific regions. Time series of these datasets can estimate seasonal variations in inundation, but are limited by the length of the acquisitions. Weekly to monthly, spatially coarser data (25 km) are available from passive microwave-based datasets such as GIEMS, SWAF and SWAMPS. Downscaling techniques have improved their spatial resolution to 90 m (GIEMS-D3) and 1 km (SWAF-HR). Hydrological models (e.g., CaMa-Flood and MGB) are capable of accurately estimating inundation over river floodplains, and at high temporal resolution depending on the input rainfall data (e.g., hourly to daily). However, they are still limited over interfluvial wetlands with less connection with rivers, unless they are upgraded for simulating 2D inundation processes and complex floodplain flow paths (Fleischmann et al., 2020; Yamazaki et al., 2014).

4.2. What are the current capabilities of flood frequency mapping?

At the basin scale, high-resolution, long-term average flood frequency can be estimated by four of the datasets analyzed here (GIEMS-D3, SWAF-HR, MGB and CaMa-Flood), with spatial resolutions ranging from 90 m to 1 km. Although multiple SAR data are currently available (e.g., Sentinel-1, ALOS-PALSAR and ALOS-2 PALSAR-2), they have a limited temporal resolution, and we still do not have a flood frequency dataset of higher spatial resolution (i.e., better than 90 m) for the whole basin based on SAR. The discrepancies among the available datasets are notable (Fig. 12). The average of the basin-scale flood frequency shows a higher agreement for areas with high flood frequency along the lower Amazon River (Fig. 12a). These are associated with a high proportion of open water areas, and have lower uncertainty (Fig. 12b). Generally, there is a smaller variation along floodplains bordering the major rivers (except for their fringes) than in interfluvial areas, especially in the Negro and Roraima wetlands (Fig. 12b). Detailed inundation mapping for the Mamirauá Sustainable Development Reserve in the Amazon mainstem floodplain (Fig. 12c) reinforces the challenges for mapping local spatio-temporal inundation dynamics. The northern part of the Mamirauá reserve has a shorter flood frequency in all datasets, while three of them (SWAF-HR, GIEMS-D3, CaMa-Flood) estimate that large portions are never flooded. For the southern part, there is some convergence for areas that are frequently flooded.

4.3. Implications for biogeochemistry, ecology and flood management

The divergent estimates of Amazon inundation extent have major implications for the quantification of the role of wetlands in global biogeochemical cycles, ecosystem processes and natural disaster management.

First, different datasets have been used to quantify the role of Amazon wetlands in the carbon cycle (Guilhen et al., 2020; Melack et al., 2004; Richey et al., 2002; Saunois et al., 2020). An intercomparison assessment of global models forced with different inundation datasets for the Amazon could provide insights into their sensitivity to the estimated inundation. This would be particularly important for modeled estimates of methane flux, given the region's significant contribution to global methane emissions from natural wetlands (Basso et al., 2021). Furthermore, for a proper estimation of methane and carbon dioxide

fluxes, dynamic inundation estimates are necessary; this study shows that most coarse-resolution dynamic datasets capture relatively well the seasonality (i.e., the timing of high and low water periods) of annual flooding at a large scale (but not at the local scales), but the magnitude of inundation area over time is still associated with significant errors (Fig. S6).

The understanding of the ecology of Amazon freshwaters has benefited from advances in remote sensing-based mapping of inundation. Hydrological variables of interest in relation to wildlife (Alvarenga et al., 2018; Bodmer et al., 2018) and vegetation distribution (Hess et al., 2015, 2003) include hydroperiod, floodplain water depth (Arantes et al., 2013; Fassoni-Andrade et al., 2020), and (lateral) surface water connectivity (Castello, 2008; Duponchelle et al., 2021; Reis et al., 2019, 2019b), and should be better estimated by future datasets. In addition, many wetland ecosystem studies are performed at the tree stand level (e.g., floristic inventories) and require high spatial resolution inundation estimates to perform meaningful spatial analyses accounting for spatial heterogeneity of wetland vegetation. Furthermore, besides a simple interfluvial/floodplain categorization of wetlands as performed here (section 3.4), which is reasonable from a hydrologic perspective, improving our understanding of the ecology of Amazon freshwater systems requires accurate mapping of habitats and their diverse vegetation types (e.g., grasslands, particular monodominant tree species, herbaceous plants). For instance, floodplain forest cover has been positively correlated to fishery yields (Arantes et al., 2018) and fish abundance (Lobón-Cerviá et al., 2015). While this wetland habitat mapping has already been done by some initiatives at the basin (Hess et al., 2015, 2003) and subregional scales (Ferreira-Ferreira et al., 2015; Silva et al., 2013), there is still a need for higher resolution and dynamic datasets.

Regarding flood monitoring in the context of natural hazard management, the flood warning systems of regional water authorities in the basin provide information based on river discharge and water level at monitoring stations (e.g., Brazil's Geological Survey SACE system; <<http://sace.cprm.gov.br/amazonas/#>>). In addition, there are other available monitoring and forecasting services that have been developed for the global scale, such as the Global Flood Detection System (<https://www.gdacs.org/flooddetection/>), based on remote sensing, and the Global Flood Monitoring System (<http://flood.umd.edu/>) and the Global Flood Awareness System (<https://www.globalfloods.eu/>), based on hydrological modeling. The currently available, basin-scale inundation datasets are unable to map flood hazard at the detailed resolution required for flood management applications, especially concerning urban areas (de Almeida et al., 2018). High-resolution flood mapping has been achieved using hydraulic modeling based on local surveys of river bathymetry and floodplain LiDAR DTM, but only for a few specific sites such as the lower Madeira River (Fleischmann et al., 2021).

4.4. Future opportunities and recommendations

Future satellite missions will provide opportunities for improved inundation mapping in the Amazon, especially the polarimetric and interferometric L-band SAR data from the upcoming NASA/ISRO mission (NISAR), the P-Band BIOMASS mission from ESA, and the Ka-band Radar Interferometer (KaRIn) swath observations from the forthcoming SWOT mission (Biancamaria et al., 2016). New inundation detection technology under development with Global Navigation Satellite System-Reflectometry (GNSS-R), such as the Cyclone GNSS (CYGNSS) constellation of GNSS-R satellites, holds promise to provide higher frequency observations of water level changes (Jensen et al., 2018; Ruf et al., 2018; Rodriguez-Alvarez et al., 2019). Further studies with the ALOS-2 PALSAR-2 data also are promising, in order to achieve new dynamic inundation detection, as well as ongoing assessments of the accuracy of the newly available high temporal resolution inundation datasets (e.g., SWAF-HR with 3-day availability). Consistent and updated validation products of Amazon inundation are required, which could

be derived from airborne, satellite, or UAV-based LiDAR surveys along multiple wetlands, in particular for overlooked wetlands such as the Negro and Roraima floodable environments where measured water levels in rivers may not adequately predict inundation area. This is especially important for the minimum inundation extent, which showed large uncertainties among the multiple datasets.

Comprehensive comparisons among multiple inundation datasets are scarce in the literature, yet are valuable ways to understand benefits and limitations of each of them. A few examples include a continental-scale assessment of flood model hazard maps in Africa (Trigg et al., 2016) and regional assessment of inundation in floodplains of Nigeria and Mozambique (Bernhofen et al., 2018), both based on global hydrological models. Similar initiatives for other areas worldwide would be welcome, especially for those that lack consistent flood mapping, such as the Congo and other large wetland systems in Africa (Papa et al., 2022). Furthermore, the combination and integration of multiple inundation datasets present a promising and effective approach (Gumbrecht et al., 2017; Hu et al., 2017). We recommend that future developments include optimal data merging approaches, e.g., by integrating inundation extent into models accounting for water cycle components with multiple constraints (Meyer Oliveira et al., 2020; Pellet et al., 2021), and by considering new types of datasets (e.g., GNSS-R; Jensen et al., 2018). Bias of different datasets could be corrected based on intercomparisons such as those we present here. For instance, recent studies have performed inundation bias correction using the Hess dataset (Aires et al., 2013; Sorribas et al., 2016). However, merging of different datasets must be performed with caution, in a consistent way, avoiding double counting of surfaces, as well as missing others: its success critically depends upon a good understanding of the limitations and assets of each individual dataset. The optimal combination of hydrological-hydraulic models with satellite flood maps using techniques such as data assimilation is also a promising alternative at the basin scale (Wongchug et al., 2020).

There is a need for the development of more large-scale 2D hydrological model applications, especially for large wetland complexes such as the Llanos de Moxos and Pacaya-Samiria, to better represent inundation dynamics (Fleischmann et al., 2020). 2D models have been applied mainly to some local-scale areas in the Amazon mainstem floodplain (Pinel et al., 2019; Rudorff et al., 2014; Trigg et al., 2009; Wilson et al., 2007). Furthermore, inundation anomalies are still poorly understood owing to the lack of ground-based inundation observations during extreme floods and droughts. Therefore, validation of estimates for extreme years has usually been performed with river water level data (in situ or from satellite altimetry) (Silva et al., 2018; Wongchug et al., 2019). Future works should address which datasets and methodologies are the most suitable for mapping extreme events. Furthermore, besides inundation extent, flood storage (Frappart et al., 2005; Papa et al., 2008; Schumann et al., 2016; Papa and Frappart, 2021) and water velocity (Pinel et al., 2019) are necessary hydraulic variables to properly address multiple environmental studies (e.g., flood monitoring, flood attenuation by floodplains, fish floodplain habitats), but to date have not been well studied in the Amazon.

Finally, there is a need for better-informed usage of the currently available inundation datasets by multiple local and regional stakeholders (e.g., local water authorities, national water agencies), as well as research communities not close to remote sensing groups. This will only be achieved through a two-way interaction with these actors and development of easy-to-access visualization platforms (i.e., investment in hydroinformatics), as well as training of regional/local user communities. To this end, we have developed a WebGIS platform (<https://amazon-inundation.herokuapp.com/>) to display and provide data acquisition links for the inundation datasets assessed here, which will be continuously updated once new datasets are made available. The interaction with local users would bring important feedback on the large-scale datasets as well, for instance through citizen science initiatives that are ongoing in the Amazon (<https://www.amazoniacienciaciudadana.org/>).

udadana.org/).

Declaration of Competing Interest

The authors declare that they have no known competing financial interests or personal relationships that could have appeared to influence the work reported in this paper.

Acknowledgments

The authors thank Dr. Fernando Jaramillo, Dr. David Kaplan, Dr. David Marques and Dr. Naziano Filizola for fruitful comments in an earlier version of this manuscript. The work was part of the SABERES project financed by the BNPParibas Foundation as part of its "Climate & Biodiversity Initiative" program 2019. A.S.F. was supported by CNPq (Conselho Nacional de Desenvolvimento Científico e Tecnológico, Brazil) [grant number 141161/2017-5]. F.P., J.F.F., M.P.B. and F.A. received support from CNES (SWOT-ST project SWOT for SOUTH AMERICA, ID: 6018-4500066497). F.P. and M.P.B. also received support from CNES (SWOT-ST project SWOT Wetlands Hydrology Monitoring). F.P. is supported by the IRD Groupe De Recherche International (GDR) SCaHyLab. J.M.M. received support from NASA IDS grant NNX17AK49G and the US National Science Foundation (Division of Environmental Biology, grant 1753856). E.P. acknowledges Nanyang Technological University (SUG-NAP EP3/19) and Ministry of Education of Singapore (AcRF Tier1 RT 06/19 and AcRF Tier2 RT 11/21). A.F.R. acknowledges the Research Foundation of São Paulo (FAPESP, grant #2019/24049-5). S.W. has been supported by the French AMANECER-MOPGA project funded by ANR and IRD (ref. ANR-18-MPGA-0008). M.C. received funding from NASA IDS grant NNX17AK49G. The SWAF dataset development was financed by the CATDS and the SWOT-AVAL programs by CNES.

Appendix A. Supplementary data

Supplementary data to this article can be found online at <https://doi.org/10.1016/j.rse.2022.113099>.

References

- Abrial, G., Martinez, J.M., Artigas, L.F., Moreira-Turcq, P., Benedetti, M.F., Vidal, L., Meziane, T., Kim, J.-H., Bernardes, M.C., Savoye, N., Deborde, J., Souza, E.L., Albéric, P., Landim de Souza, M.F., Roland, F., 2014. Amazon River carbon dioxide outgassing fuelled by wetlands. *Nature* 505, 395–398. <https://doi.org/10.1038/nature12797>.
- Aires, F., Papa, F., Prigent, C., 2013. A long-term, high-resolution wetland dataset over the Amazon Basin, downsampled from a multiwavelength retrieval using SAR data. *J. Hydrometeorol.* 14, 594–607. <https://doi.org/10.1175/JHM-D-12-093.1>.
- Aires, F., Miolane, L., Prigent, C., Pham, B., Fluet-Chouinard, E., Lehner, B., Papa, F., 2017. A global dynamic long-term inundation extent dataset at high spatial resolution derived through downscaling of satellite observations. *J. Hydrometeorol.* 18, 1305–1325. <https://doi.org/10.1175/JHM-D-16-0155.1>.
- Aires, F., Prigent, C., Fluet-Chouinard, E., Yamazaki, D., Papa, F., Lehner, B., 2018. Comparison of visible and multi-satellite global inundation datasets at high-spatial resolution. *Remote Sens. Environ.* 216, 427–441. <https://doi.org/10.1016/j.rse.2018.06.015>.
- Al Bitar, A., Parrens, M., Fatras, C., Luque, S.P., 2020. Global weekly inland surface water dynamics from L-band microwave. In: IGARSS 2020–2020 IEEE International Geoscience and Remote Sensing Symposium, pp. 5089–5092.
- Alsdorf, D., Bates, P., Melack, J., Wilson, M., Dunne, T., 2007. Spatial and temporal complexity of the Amazon flood measured from space. *Geophys. Res. Lett.* 34. <https://doi.org/10.1029/2007GL029447>.
- Alvarenga, G.C., Ramalho, E.E., Baccaro, F.B., da Rocha, D.G., Ferreira-Ferreira, J., Dinelli Bobrowiec, P.E., 2018. Spatial patterns of medium and large size mammal assemblages in várzea and terra firme forests, Central Amazonia, Brazil. *PLoS One* 13, 1–19. <https://doi.org/10.1371/journal.pone.0198120>.
- Arantes, C.C., Castello, L., Cetra, M., Schilling, A., 2013. Environmental influences on the distribution of arapaima in Amazon floodplains. *Environ. Biol. Fish.* 96, 1257–1267. <https://doi.org/10.1007/s10641-011-9917-9>.
- Arantes, C.C., Winemiller, K.O., Petre, M., Castello, L., Hess, L.L., Freitas, C.E.C., 2018. Relationships between forest cover and fish diversity in the Amazon River floodplain. *J. Appl. Ecol.* 55, 386–395. <https://doi.org/10.1111/1365-2664.12967>.
- Armijos, E., Crave, A., Espinoza, J.C., Filizola, N., Espinoza-Villar, R., Ayes Fonseca, P., Fraizy, P., Gutierrez, O., Vauchel, P., Camenen, B., Martinez, J.M., Dos Santos, A.,

Santini, W., Cochonneau, G., Guyot, J.L., 2020. Rainfall control on Amazon sediment flux: synthesis from 20 years of monitoring. *Environ. Res. Commun.* 2, 051008. <https://doi.org/10.1088/2515-7620/ab9003>.

Arnesen, A.S., Silva, T.S.F., Hess, L.L., Novo, E.M.L.M., Rudorff, C.M., Chapman, B.D., McDonald, K.C., 2013. Monitoring flood extent in the lower Amazon River floodplain using ALOS/PALSAR ScanSAR images. *Remote Sens. Environ.* 130, 51–61. <https://doi.org/10.1016/j.rse.2012.10.035>.

Asner, G.P., 2001. Cloud cover in Landsat observations of the Brazilian Amazon. *Int. J. Remote Sens.* 22, 3855–3862. <https://doi.org/10.1080/01431160010006926>.

Balsamo, G., Beljaars, A., Scipal, K., Viterbo, P., van den Hurk, B., Hirschi, M., Betts, A.K., 2009. A revised hydrology for the ECMWF model: verification from field site to terrestrial water storage and impact in the integrated forecast system. *J. Hydrometeorol.* 10, 623–643. <https://doi.org/10.1175/2008jhm1068.1>.

Barichivich, J., Gloor, E., Peylin, P., Brienen, R.J.W., Schöngart, J., Espinoza, J.C., Pattnayak, K.C., 2018. Recent intensification of Amazon flooding extremes driven by strengthened Walker circulation. *Sci. Adv.* 4 <https://doi.org/10.1126/sciadv.aat8785>.

Basso, L.S., Marani, L., Gatti, L.V., Miller, J.B., Gloor, M., Melack, J., Cassol, H.L.G., Tejada, G., Domingues, L.G., Arai, E., Sanchez, A.H., Corrêa, S.M., Anderson, L., Aragão, L.E.O.C., Correia, C.S.C., Crispim, S.P., Neves, R.A.L., 2021. Amazon methane budget derived from multi-year airborne observations highlights regional variations in emissions. *Commun. Earth Environ.* 2, 1–14. <https://doi.org/10.1038/s43247-021-00314-4>.

Bates, P.D., De Roo, A.P.J., 2000. A simple raster-based model for flood inundation simulation. *J. Hydrol.* [https://doi.org/10.1016/S0022-1694\(00\)00278-X](https://doi.org/10.1016/S0022-1694(00)00278-X).

Beck, H.E., Van Dijk, A.I.J.M., Levizzani, V., Schellekens, J., Miralles, D.G., Martens, B., De Roo, A., 2017. MSWEP: 3-hourly 0.25° global gridded precipitation (1979–2015) by merging gauge, satellite, and reanalysis data. *Hydrol. Earth Syst. Sci.* <https://doi.org/10.5194/hess-21-589-2017>.

Beighley, R.E., Eggert, K.G., Dunne, T., He, Y., Gummadi, V., Verdin, K.L., 2009. Simulating hydrologic and hydraulic processes throughout the Amazon River basin. *Hydrol. Process.* 23, 1221–1235. <https://doi.org/10.1002/hyp.7252>.

Belger, L., Forsberg, B.R., Melack, J.M., 2011. Carbon dioxide and methane emissions from interfluvial wetlands in the upper Negro River basin, Brazil. *Biogeochemistry* 105, 171–183. <https://doi.org/10.1007/s10533-010-9536-0>.

Bernhofen, M.V., Whyman, C., Trigg, M.A., Sleigh, P.A., Smith, A.M., Sampson, C.C., Yamazaki, D., Ward, P.J., Rudari, R., Pappenberg, F., Dottori, F., Salomon, P., Winsemius, H.C., 2018. A first collective validation of global fluvial flood models for major floods in Nigeria and Mozambique. *Environ. Res. Lett.* 13, 104007 <https://doi.org/10.1088/1748-9326/aae014>.

Biancamaria, S., Lettenmaier, D.P., Pavelsky, T.M., 2016. The SWOT mission and its capabilities for land hydrology. *Surv. Geophys.* 37, 307–337. <https://doi.org/10.1007/s10712-015-9346-y>.

Blatrix, R., Roux, B., Béarez, P., Prestes-Carneiro, G., Amaya, M., Aramayo, J.L., Rodrigues, L., Lombardo, U., Iriarte, J., De Souza, J.G., Robinson, M., Bernard, C., Pouilly, M., Durécu, M., Huchzermeyer, C.F., Kalebe, M., Ovando, A., McKey, D., 2018. The unique functioning of a pre-Columbian Amazonian floodplain fishery. *Sci. Rep.* 8 <https://doi.org/10.1038/s41598-018-24454-4>.

Bodmer, R., Mayor, P., Antunes, M., Chota, K., Fang, T., Puertas, P., Pittet, M., Kirkland, M., Walkey, M., Rios, C., Perez-Peña, P., Henderson, P., Bodmer, W., Bicerra, A., Zegarra, J., Docherty, E., 2018. Major shifts in Amazon wildlife populations from recent intensification of floods and drought. *Conserv. Biol.* 32, 333–344. <https://doi.org/10.1111/cobi.12993>.

Bonnet, M.P., Pinel, S., Garnier, J., Bois, J., Resende Boaventura, G., Seyler, P., Motta Marques, D., 2017. Amazonian floodplain water balance based on modelling and analyses of hydrologic and electrical conductivity data. *Hydrol. Process.* 31, 1702–1718. <https://doi.org/10.1002/hyp.11138>.

Bontemps, S., Defourny, P., Radoux, J., Van Bogaert, E., Lamarche, C., Achard, F., Mayaux, P., Boettcher, M., Brockmann, C., Kirches, G., 2013. Consistent global land cover maps for climate modelling communities: current achievements of the ESA's land cover CCI. In: *Proceedings of the ESA Living Planet Symposium*. Edinburgh.

Bourrel, L., Phillips, L., Moreau, S., 2008. The dynamics of floods in the Bolivian Amazon Basin. *Hydrol. Process.* 23, 3161–3167. <https://doi.org/10.1002/hyp.7384>.

Castello, L., 2008. Lateral migration of *Arapaima gigas* in floodplains of the Amazon. *Ecol. Freshw. Fish* 17, 38–46. <https://doi.org/10.1111/j.1600-0633.2007.00255.x>.

Chapman, B., McDonald, K., Shimada, M., Rosengqvist, A., Schroeder, R., Hess, L., 2015. Mapping regional inundation with Spaceborne L-band SAR. *Remote Sens.* 7, 5440–5470. <https://doi.org/10.3390/rs70505440>.

Coe, M.T., Costa, M.H., Howard, E.A., 2008. Simulating the surface waters of the Amazon River basin: impacts of new river geomorphic and flow parameterizations. *Hydrol. Process.* 22, 2542–2553. <https://doi.org/10.1002/hyp.6850>.

Coomes, O.T., Lapointe, M., Templeton, M., List, G., 2016. Amazon river flow regime and flood recession agriculture: flood stage reversals and risk of annual crop loss. *J. Hydrol.* 539, 214–222. <https://doi.org/10.1016/j.jhydrol.2016.05.027>.

da Paca, V.H.M., Espinoza-Dávalos, G.E., Hessels, T.M., Moreira, D.M., Comair, G.F., Bastiaanssen, W.G.M., 2019. The spatial variability of actual evapotranspiration across the Amazon River basin based on remote sensing products validated with flux towers. *Ecol. Process.* 8, 6. <https://doi.org/10.1186/s13717-019-0158-8>.

de Almeida, G.A.M., Bates, P., Ozdemir, H., 2018. Modelling urban floods at submetre resolution: challenges or opportunities for flood risk management? *J. Flood Risk Manag.* 11, S855–S865. <https://doi.org/10.1111/jfr3.12276>.

de Resende, A.F., Schöngart, J., Streher, A.S., Ferreira-Ferreira, J., Piedade, M.T.F., Silva, T.S.F., 2019. Massive tree mortality from flood pulse disturbances in Amazonian floodplain forests: the collateral effects of hydropower production. *Sci. Total Environ.* 659, 587–598. <https://doi.org/10.1016/j.scitotenv.2018.12.208>.

Denevan, W.M., 1996. A bluff model of riverine settlement in prehistoric Amazonia. *Ann. Assoc. Am. Geogr.* 86, 654–681. <https://doi.org/10.1111/j.1467-8306.1996.tb01771.x>.

Draper, F.C., Roucoux, K.H., Lawson, I.T., Mitchard, E.T.A., Honorio Coronado, E.N., Lähdeoja, O., Montenegro, L.T., Sandoval, E.V., Zarate, R., Baker, T.R., 2014. The distribution and amount of carbon in the largest peatland complex in Amazonia. *Environ. Res. Lett.* 9 <https://doi.org/10.1088/1748-9326/9/12/124017>.

Dunne, T., Mertes, L.A.K., Meade, R.H., Richey, J.E., Forsberg, B.R., 1998. Exchanges of sediment between the flood plain and channel of the Amazon River in Brazil. *Bull. Geol. Soc. Am.* 110, 450–467. [https://doi.org/10.1130/0016-7606\(1998\)110<450:EOSBT>2.3.CO;2](https://doi.org/10.1130/0016-7606(1998)110<450:EOSBT>2.3.CO;2).

Duponchelle, F., Isaac, V.J., Doria, C., Van Damme, P.A., Herrera-R, G.A., Anderson, E.P., Cruz, R.E.A., Hauser, M., Hermann, T.W., Agudelo, E., Bonilla-Castillo, C., Barthem, R., Freitas, C.E.C., García-Dávila, C., García-Vasquez, A., Renno, J., Castello, L., 2021. Conservation of migratory fishes in the Amazon basin. *Aquat. Conserv. Mar. Freshwat. Ecosyst.* <https://doi.org/10.1002/aqc.3550>.

Espinoza Villar, J.C., Ronchail, J., Guyot, J.L., Cochonneau, G., Naziano, F., Lavado, W., De Oliveira, E., Pombosa, R., Vauchel, P., 2009. Spatio-temporal rainfall variability in the Amazon basin countries (Brazil, Peru, Bolivia, Colombia, and Ecuador). *Int. J. Climatol.* 29, 1574–1594. <https://doi.org/10.1002/joc.1791>.

Espinoza Villar, J.C., Ronchail, J., Marenco, J.A., Segura, H., 2019. Contrasting North–South changes in Amazon wet-day and dry-day frequency and related atmospheric features (1981–2017). *Clim. Dyn.* 52, 5413–5430. <https://doi.org/10.1007/s00382-018-4462-2>.

Farr, T.G., Rosen, P.A., Caro, E., Crippen, R., Duren, R., Hensley, S., Kobrick, M., Paller, M., Rodriguez, E., Roth, L., Seal, D., Shaffer, S., Shimada, J., Umland, J., Werner, M., Oskin, M., Burbank, D., Alsdorf, D.E., 2007. The shuttle radar topography mission. *Rev. Geophys.* 45, 1–25. <https://doi.org/10.1029/2005RG000183>.

Fassoni-Andrade, 2020. Mapeamento e caracterização do sistema rio-planície da Amazônia central via sensoriamento remoto e modelagem hidráulica. Federal University of Rio Grande do Sul. PhD thesis. Available at: <https://lume.ufrgs.br/handle/10183/211269>.

Fassoni-Andrade, A.C., de Paiva, R.C.D., 2019. Mapping spatial-temporal sediment dynamics of river-floodplains in the Amazon. *Remote Sens. Environ.* <https://doi.org/10.1016/j.rse.2018.10.038>.

Fassoni-Andrade, A.C., de Paiva, R.C.D., de Rudorff, C.M., Barbosa, C.C.F., de Novo, E.M. L.M., 2020. High-resolution mapping of floodplain topography from space: a case study in the Amazon. *Remote Sens. Environ.* 251, 112065 <https://doi.org/10.1016/j.rse.2020.112065>.

Fassoni-Andrade, A.C., Fleischmann, A.S., Papa, F., de Paiva, R.C.D., Wongchuig, S., Melack, J.M., Moreira, A.A., Paris, A., Ruhoff, A., Barbosa, C., Maciel, D.A., Novo, E., Durand, F., Frappart, F., Aires, F., Abrahão, G.M., Ferreira-Ferreira, J., Espinoza, J. C., Laipelt, L., Costa, M.H., Espinoza-Villar, R., Calmant, S., Pellet, V., 2021. Amazon hydrology from space: scientific advances and future challenges. *Rev. Geophys.* 59, 1–97. <https://doi.org/10.1029/2020RG000728>.

Feng, D., Raoufi, R., Beighley, E., Melack, J.M., Goulding, M., Barthem, R.B., Venticinque, E., Cañas, C., Forsberg, B., Sorribas, M.V., 2020. Future climate impacts on the hydrology of headwater streams in the Amazon River basin: implications for migratory goliath catfishes. *Hydrol. Process.* <https://doi.org/10.1002/hyp.13952>.

Ferreira-Ferreira, J., Silva, T.S.F., Streher, A.S., Affonso, A.G., de Almeida Furtado, L.F., Forsberg, B.R., Valsecchi, J., Queiroz, H.L., de Moraes Novo, E.M.L., 2015. Combining ALOS/PALSAR derived vegetation structure and inundation patterns to characterize major vegetation types in the Mamirauá sustainable development reserve, Central Amazon floodplain, Brazil. *Wetl. Ecol. Manag.* 23, 41–59. <https://doi.org/10.1007/s11273-014-9359-1>.

Fleischmann, A.S., Paiva, R.C.D., Collischonn, W., Siqueira, V.A., Paris, A., Moreira, D. M., Papa, F., Bitar, A.A., Parrens, M., Aires, F., Garambois, P.A., 2020. Trade-offs between 1-D and 2-D regional river hydrodynamic models. *Water Resour. Res.* 56 <https://doi.org/10.1029/2019WR026812>.

Fleischmann, A.S., Fialho Bréda, J.P., Rudorff, C., de Dias Paiva, R.C., Collischonn, W., Papa, F., Ravanello, M.M., 2021. River Flood modeling and remote sensing across scales: Lessons from Brazil. In: Schumann, G.J.P. (Ed.), *Earth Observation for Flood Applications*. Elsevier, pp. 61–103. <https://doi.org/10.1016/B978-0-12-819412-6.00004-3>.

Flores, B.M., Holmgren, M., 2021. White-sand savannas expand at the core of the Amazon after forest wildfires. *Ecosystems* 24, 1624–1637. <https://doi.org/10.1007/s10021-021-00607-x>.

Fluet-Chouinard, E., Lehner, B., Rebelo, L.M., Papa, F., Hamilton, S.K., 2015. Development of a global inundation map at high spatial resolution from topographic downscaling of coarse-scale remote sensing data. *Remote Sens. Environ.* 158, 348–361. <https://doi.org/10.1016/j.rse.2014.10.015>.

Frappart, F., Seyler, F., Martinez, J., León, J.G., Cazenave, A., 2005. Floodplain water storage in the Negro River basin estimated from microwave remote sensing of inundation area and water levels. *Remote Sens. Environ.* 99, 387–399. <https://doi.org/10.1016/j.rse.2005.08.016>.

Fu, R., Yin, L., Li, W., Arias, P.A., Dickinson, R.E., Huang, L., Chakraborty, S., Fernandes, K., Liebmann, B., Fisher, R., Myneni, R.B., 2013. Increased dry-season length over southern Amazonia in recent decades and its implication for future climate projection. *Proc. Natl. Acad. Sci. U. S. A.* 110, 18110–18115. <https://doi.org/10.1073/pnas.1302584110>.

Getirana, A., Boone, A., Yamazaki, D., Decharme, B., Papa, F., Mognard, N., 2012. The hydrological modeling and analysis platform (HyMAP): evaluation in the Amazon Basin. *J. Hydrometeorol.* 13, 1641–1665. <https://doi.org/10.1175/JHM-D-12-021.1>.

Getirana, A., Peters-Lidard, C., Rodell, M., Bates, P.D., 2017. Trade-off between cost and accuracy in large-scale surface water dynamic modeling. *Water Resour. Res.* 53, 4942–4955. <https://doi.org/10.1002/2017WR020519>.

Gloos, M., Brienen, R.J.W., Galbraith, D., Feldpausch, T.R., Schöngart, J., Guyot, J.L., Espinoza, J.C., Lloyd, J., Phillips, O.L., 2013. Intensification of the Amazon hydrological cycle over the last two decades. *Geophys. Res. Lett.* 40, 1729–1733. <https://doi.org/10.1002/grl.50377>.

Guilhen, J., Al Bitar, A., Sauvage, S., Parrens, M., Martinez, J., Abril, G., Moreira-Turcq, P., Sánchez-Pérez, J.-M., 2020. Denitrification and associated nitrous oxide and carbon dioxide emissions from the Amazonian wetlands. *Biogeosciences* 17, 4297–4311. <https://doi.org/10.5194/bg-17-4297-2020>.

Gumbrecht, T., Roman-Cuesta, R.M., Verchot, L., Herold, M., Wittmann, F., Householder, E., Herold, N., Murdaryso, D., 2017. An expert system model for mapping tropical wetlands and peatlands reveals South America as the largest contributor. *Glob. Chang. Biol.* 23, 3581–3599. <https://doi.org/10.1111/gcb.13689>.

Hamilton, S.K., Sippel, S.J., Melack, J.M., 2002. Comparison of inundation patterns among major South American floodplains. *J. Geophys. Res.* 107, 1–14. <https://doi.org/10.1029/2000JD000306107> (D20): Art. No. 8038.

Hamilton, S.K., Sippel, S.J., Melack, J.M., 2004. Seasonal inundation patterns in two large savanna floodplains of South America: the Llanos de Mojos (Bolivia) and the Llanos del Orinoco (Venezuela and Colombia). *Hydrol. Process.* 18, 2103–2116. <https://doi.org/10.1002/hyp.5559>.

Hamilton, S.K., Kellndorfer, J., Lehner, B., Tobler, M., 2007. Remote sensing of floodplain geomorphology as a surrogate for biodiversity in a tropical river system (Madre de Dios, Peru). *Geomorphology* 89, 23–38. <https://doi.org/10.1016/j.geomorph.2006.07.024>.

Hansen, M.C., Potapov, P.V., Moore, R., Hancher, M., Turubanova, S.A., Tyukavina, A., Thau, D., Stehman, S.V., Goetz, S.J., Loveland, T.R., Kommareddy, A., Egorov, A., Chini, L., Justice, C.O., Townshend, J.R.G., 2013. High-resolution global maps of 21st-century forest cover change. *Science* 342, 850–853. <https://doi.org/10.1126/science.1244693>.

Harris, I., Jones, P.D., Osborn, T.J., Lister, D.H., 2014. Updated high-resolution grids of monthly climatic observations - the CRU TS3.10 dataset. *Int. J. Climatol.* 34, 623–642. <https://doi.org/10.1002/joc.3711>.

Hawes, J.E., Peres, C.A., Riley, L.B., Hess, L.L., 2012. Landscape-scale variation in structure and biomass of Amazonian seasonally flooded and unflooded forests. *For. Ecol. Manag.* 281, 163–176. <https://doi.org/10.1016/j.foreco.2012.06.023>.

Hess, L.L., Melack, J.M., Novo, E.M.L.M., Barbosa, C.C.F., Gastil, M., 2003. Dual-season mapping of wetland inundation and vegetation for the Central Amazon basin. *Remote Sens. Environ.* 87, 404–428. <https://doi.org/10.1016/j.rse.2003.04.001>.

Hess, L.L., Melack, J.M., Affonso, A.G., Barbosa, C., Gastil-Buhl, M., Novo, E.M.L.M., 2015. Wetlands of the lowland Amazon Basin: extent, vegetative cover, and dual-season inundated area as mapped with JERS-1 synthetic aperture radar. *Wetlands* 35, 745–756. <https://doi.org/10.1007/s13157-015-0666-y>.

Hoch, J.M., Haag, A.V., Van Dam, A., Winsemius, H.C., Van Beek, L.P.H., Bierkens, M.F.P., 2017. Assessing the impact of hydrodynamics on large-scale flood wave propagation: a case study for the Amazon Basin. *Hydrol. Earth Syst. Sci.* 21, 117–132. <https://doi.org/10.5194/hess-21-117-2017>.

Hu, S., Niu, Z., Chen, Y., 2017. Global wetland datasets: a review. *Wetlands* 37, 807–817. <https://doi.org/10.1007/s13157-017-0927-z>.

Jardim, C.M., Nardoto, G.B., de Lima, A.C.B., de Jesus Silva, R., Schor, T., de Oliveira, J.A., Martinelli, L.A., 2020. The influence of seasonal river flooding in food consumption of riverine dwellers in the Central Amazon region: an isotopic approach. *Archaeol. Anthropol. Sci.* 12 <https://doi.org/10.1007/s12520-020-01172-5>.

Jensen, K., McDonald, K., 2019. Surface water microwave product series version 3: a near-real time and 25-year historical global inundated area fraction time series from active and passive microwave remote sensing. *IEEE Geosci. Remote Sens. Lett.* 16, 1402–1406. <https://doi.org/10.1109/lgrs.2019.2898779>.

Jensen, K., McDonald, K., Podest, E., Rodriguez-Alvarez, N., Horna, V., Steiner, N., 2018. Assessing L-band GNSS-reflectometry and imaging radar for detecting sub-canopy inundation dynamics in a tropical wetlands complex. *Remote Sens.* 10, 1431. <https://doi.org/10.3390/rs10091431>.

Ji, X., Lesack, L.F.W., Melack, J.M., Wang, S., Riley, W.J., Shen, C., 2019. Seasonal and interannual patterns and controls of hydrological fluxes in an Amazon floodplain lake with a surface-subsurface process model. *Water Resour. Res.* 55, 3056–3075. <https://doi.org/10.1029/2018WR023897>.

Junk, W.J., Bayley, P.B., Sparks, R.E., 1989. The flood pulse concept in river-floodplain systems. *Can. Spec. Publ. Fish. Aquatic Sci.* 106 (1), 110–127.

Junk, W.J., Furch, K., Limnologie, M., Tropenökologie, A., Plon, W., 1993. A general review of tropical South American floodplains. *Wetl. Ecol. Manag.* 2, 231–238.

Junk, W.J., Piedade, M.T.F., Schöngart, J., Cohn-Haft, M., Adeney, J.M., Wittmann, F., 2011. A classification of major naturally-occurring Amazonian lowland wetlands. *Wetlands* 31, 623–640. <https://doi.org/10.1007/s13157-011-0190-7>.

Látheenoja, O., Reátegui, Y.R., Räsänen, M., Torres, D.D.C., Oinonen, M., Page, S., 2012. The large Amazonian peatland carbon sink in the subsiding Pastaza-Marañón foreland basin, Peru. *Glob. Chang. Biol.* 18, 164–178. <https://doi.org/10.1111/j.1365-2486.2011.02504.x>.

Latrubesse, E.M., 2012. Amazon lakes. In: Encyclopedia of Earth Sciences Series. https://doi.org/10.1007/978-1-4020-4410-6_36.

Lehner, B., Döll, P., 2004. Development and validation of a global database of lakes, reservoirs and wetlands. *J. Hydrol.* 296, 1–22. <https://doi.org/10.1016/j.jhydrol.2004.03.028>.

Lehner, B., Grill, G., 2013. Global river hydrography and network routing: baseline data and new approaches to study the world's large river systems. *Hydrol. Process.* <https://doi.org/10.1002/hyp.9740>.

Lobón-Cerviá, J., Hess, L.L., Melack, J.M., Araujo-Lima, C.A.R.M., 2015. The importance of forest cover for fish richness and abundance on the Amazon floodplain. *Hydrobiologia* 750, 245–255. <https://doi.org/10.1007/s10750-014-2040-0>.

Luize, B.G., Silva, T.S.F., Wittmann, F., Assis, R.L., Venticinque, E.M., 2015. Effects of the flooding gradient on tree community diversity in Várzea forests of the Purus River, Central Amazon, Brazil. *Biotropica* 47, 137–142. <https://doi.org/10.1111/btr.12203>.

Luo, X., Li, H.-Y., Leung, L.R., Tesfa, T.K., Getirana, A., Papa, F., Hess, L.L., 2017. Modeling surface water dynamics in the Amazon Basin using MOSART-inundation v1.0: impacts of geomorphological parameters and river flow representation. *Geosci. Model Dev.* 10, 1233–1259. <https://doi.org/10.5194/gmd-10-1233-2017>.

Martínez-Espinosa, C., Sauvage, S., Al Bitar, A., Green, P.A., Vörösmarty, C.J., Sánchez-Pérez, J.M., 2020. Denitrification in wetlands: a review towards a quantification at global scale. *Sci. Total Environ.* 754, 142398. <https://doi.org/10.1016/j.scitotenv.2020.142398>.

Matthews, E., Fung, I., 1987. Methane emission from natural wetlands: global distribution, area, and environmental characteristics of sources. *Glob. Biogeochem. Cycles* 1, 61–86. <https://doi.org/10.1029/GB001i001p00061>.

Melack, J.M., 2016. Aquatic ecosystems. *Ecol. Stud.* 119–148. https://doi.org/10.1007/978-3-662-49902-3_7.

Melack, J.M., Coe, M.T., 2021. Amazon floodplain hydrology and implications for aquatic conservation. *Aquat. Conserv. Mar. Freshwat. Ecosyst.* 1029–1040. <https://doi.org/10.1002/aqc.3558>.

Melack, J.M., Forsberg, B.R., 2001. Biogeochemistry of Amazon floodplain. In: McClain, M.E., Victoria, R., Richey, J.E. (Eds.), *The Biogeochemistry of the Amazon Basin*. Oxford University Press, New York, USA.

Melack, J.M., Hess, L.L., 2010. Remote sensing of the distribution and extent of wetlands in the Amazon Basin. In: *Amazonian Floodplain Forests*, pp. 43–59. https://doi.org/10.1007/978-90-481-8725-6_3.

Melack, J.M., Hess, L.L., Gastil, M., Forsberg, B.R., Hamilton, S.K., Lima, I.B.T., Novo, E.M.L.M., 2004. Regionalization of methane emissions in the Amazon Basin with microwave remote sensing. *Glob. Chang. Biol.* 10, 530–544. <https://doi.org/10.1111/j.1365-2486.2004.00763.x>.

Meyer Oliveira, A., Fleischmann, A., Paiva, R., 2020. On the contribution of remote sensing-based calibration to model multiple hydrological variables. *J. Hydrol.* <https://doi.org/10.1016/j.jhydrol.2021.126184>.

Miguez-Macho, G., Fan, Y., 2012. The role of groundwater in the Amazon water cycle: 1. Influence on seasonal streamflow, flooding and wetlands. *J. Geophys. Res. Atmos.* 117, 1–30. <https://doi.org/10.1029/2012JD017539>.

O'Loughlin, F.E., Paiva, R.C.D., Durand, M., Alsdorf, D.E., Bates, P.D., 2016. A multi-sensor approach towards a global vegetation corrected SRTM DEM product. *Remote Sens. Environ.* 182, 49–59. <https://doi.org/10.1016/j.rse.2016.04.018>.

Ovando, A., Tomasella, J., Rodriguez, D.A., Martinez, J.M., Siqueira-Junior, J.L., Pinto, G.L.N., Passy, P., Vauchel, P., Noriega, L., von Randow, C., 2016. Extreme flood events in the Bolivian Amazon wetlands. *J. Hydrol. Reg. Stud.* 5, 293–308. <https://doi.org/10.1016/j.ejrh.2015.11.004>.

Ovando, A., Martinez, J.M., Tomasella, J., Rodriguez, D.A., von Randow, C., 2018. Multi-temporal flood mapping and satellite altimetry used to evaluate the flood dynamics of the Bolivian Amazon wetlands. *Int. J. Appl. Earth Obs. Geoinf.* 69, 27–40. <https://doi.org/10.1016/j.jag.2018.02.013>.

Paiva, R., Buarque, D.C., Collischonn, W., Bonnet, M.P., Frappart, F., Calmant, S., Bulhões Mendes, C.A., 2013. Large-scale hydrologic and hydrodynamic modeling of the Amazon River basin. *Water Resour. Res.* 49, 1226–1243. <https://doi.org/10.1002/wrcr.20067>.

Pangala, S.R., Enrich-Prast, A., Basso, L.S., Peixoto, R.B., Bastviken, D., Hornbrook, E.R.C., Gatti, L.V., Marotta, H., Calazans, L.S.B., Sakuragi, C.M., Bastos, W.R., Malm, O., Gloor, E., Miller, J.B., Gauci, V., 2017. Large emissions from floodplain trees close the Amazon methane budget. *Nature* 552, 230–234. <https://doi.org/10.1038/nature24639>.

Papa, F., Frappart, F., 2021. Surface water storage in rivers and wetlands derived from satellite observations: a review of current advances and future opportunities for hydrological sciences. *Remote Sens.* 13 (20), 4162. <https://doi.org/10.3390/rs13204162>.

Papa, F., Güntner, A., Frappart, F., Prigent, C., Rossow, W.B., 2008. Variations of surface water extent and water storage in large river basins: a comparison of different global data sources. *Geophys. Res. Lett.* 35, L11401. <https://doi.org/10.1029/2008GL033857>.

Papa, F., Frappart, F., Caires, F., Aires, F., Jimenez, C., Rossow, W.B., Matthews, E., 2010. Interannual variability of surface water extent at the global scale, 1993–2004. *J. Geophys. Res.* 115, D12111. <https://doi.org/10.1029/2009JD012674>.

Papa, F., Crétaux, J.-F., Grippa, M., Robert, E., Trigg, M., Tshimanga, R., Kitambo, B., Paris, O., Carr, A., Fleischmann, A.S., de Fleury, M., Gbetkom, P.G., Calmettes, B., Calmant, S., 2022. Water resources in Africa under global change: monitoring surface waters from space. *Surv. Geophys.* <https://doi.org/10.1007/s10712-022-09700-9>.

Park, E., Latrubesse, E.M., 2017. The hydro-geomorphologic complexity of the lower Amazon River floodplain and hydrological connectivity assessed by remote sensing and field control. *Remote Sens. Environ.* 198, 321–332. <https://doi.org/10.1016/j.rse.2017.06.021>.

Park, E., Latrubesse, E.M., 2019. A geomorphological assessment of wash-load sediment fluxes and floodplain sediment sinks along the lower Amazon River. *Geology* 47, 403–406. <https://doi.org/10.1130/G45769.1>.

Parrens, M., Al Bitar, A., Frappart, F., Papa, F., Calmant, S., Crétaux, J.-F., Wigneron, J.-P., Kerr, Y., 2017. Mapping dynamic water fraction under the tropical rain forests of the Amazonian basin from SMOS brightness temperatures. *Water* 9, 350. <https://doi.org/10.3390/w9050350>.

Parrens, M., Al Bitar, A., Frappart, F., Paiva, R., Wongchuig, S., Papa, F., Yamasaki, D., Kerr, Y., 2019. High resolution mapping of inundation area in the Amazon basin from a combination of L-band passive microwave, optical and radar datasets. *Int. J. Appl. Earth Obs. Geoinf.* 81, 58–71. <https://doi.org/10.1016/j.jag.2019.04.011>.

Pekel, J., Cottam, A., Gorelick, N., Belward, A.S., 2016. High-resolution mapping of global surface water and its long-term changes. *Nature* 540, 418–422. <https://doi.org/10.1038/nature20584>.

Pellet, V., Aires, F., Yamazaki, D., Papa, F., 2021. Coherent satellite monitoring of the water cycle over the Amazon. Part 1: methodology and initial evaluation. *Water Resour. Res.* 57, 1–21. <https://doi.org/10.1029/2020wr028647>.

Pham-Duc, B., Prigent, C., Aires, F., Papa, F., 2017. Comparisons of global terrestrial surface water datasets over 15 years. *J. Hydrometeorol.* 18, 993–1007. <https://doi.org/10.1175/JHM-D-16-0206.1>.

Pickens, A.H., Hansen, M.C., Hancher, M., Stehman, S.V., Tyukavina, A., Potapov, P., Marroquin, B., Sherani, Z., 2020. Mapping and sampling to characterize global inland water dynamics from 1999 to 2018 with full Landsat time-series. *Remote Sens. Environ.* 243, 111792. <https://doi.org/10.1016/j.rse.2020.111792>.

Pinel, S., Bonnet, M., Da Silva, S.J., Sampaio, T.C., Garnier, J., Catry, T., Calmant, S., Fragoso, C.R., Moreira, D., Motta Marques, D., Seyler, F., 2019. Flooding dynamics within an Amazonian floodplain: water circulation patterns and inundation duration. *Water Resour. Res.* <https://doi.org/10.1029/2019WR026081>, 2019WR026081.

Prigent, C., Matthews, E., Aires, F., Rossow, W.B., 2001. Remote sensing of global wetland dynamics with multiple satellite data sets. *Geophys. Res. Lett.* 28, 4631–4634. <https://doi.org/10.1029/2001GL013263>.

Prigent, C., Papa, F., Aires, F., Rossow, W.B., Matthews, E., 2007. Global inundation dynamics inferred from multiple satellite observations, 1993–2000. *J. Geophys. Res. Atmos.* 112, 1993–2000. <https://doi.org/10.1029/2006JD007847>.

Prigent, C., Rochetin, N., Aires, F., Defer, E., Grandpeix, J.-Y., Jimenez, C., Papa, F., 2011. Impact of the inundation occurrence on the deep convection at continental scale from satellite observations and modeling experiments. *J. Geophys. Res. Atmos.* 116. <https://doi.org/10.1029/2011JD016311> n/a-n/a.

Prigent, C., Jimenez, C., Bousquet, P., 2020. Satellite-derived global surface water extent and dynamics over the last 25 years (GIEMS-2). *J. Geophys. Res. Atmos.* 125, 1–18. <https://doi.org/10.1029/2019JD030711>.

Reis, V., Hermoso, V., Hamilton, S.K., Bunn, S.E., Fluet-Chouinard, E., Venables, B., Linke, S., 2019a. Characterizing seasonal dynamics of Amazonian wetlands for conservation and decision making. *Aquat. Conserv. Mar. Freshwat. Ecosyst.* 29, 1073–1082. <https://doi.org/10.1002/aqc.3051>.

Reis, V., Hermoso, V., Hamilton, S.K., Bunn, S.E., Linke, S., 2019b. Conservation planning for river-wetland mosaics: a flexible spatial approach to integrate floodplain and upstream catchment connectivity. *Biol. Conserv.* 236, 356–365. <https://doi.org/10.1016/j.biocon.2019.05.042>.

Rennó, C.D., Nobre, A.D., Cuartas, L.A., Soares, J.V., Hodnett, M.G., Tomasella, J., Waterlo, M.J., 2008. HAND, a new terrain descriptor using SRTM-DEM: mapping terra-firme rainforest environments in Amazonia. *Remote Sens. Environ.* 112, 3469–3481. <https://doi.org/10.1016/j.rse.2008.03.018>.

Renó, V.F., Novo, E.M.L.M., Suemitsu, C., Rennó, C.D., Silva, T.S.F., 2011. Assessment of deforestation in the lower Amazon floodplain using historical Landsat MSS/TM imagery. *Remote Sens. Environ.* 115, 3446–3456. <https://doi.org/10.1016/j.rse.2011.08.008>.

Restrepo, A., Kettner, A.J., Robert Brakenridge, G., 2020. Monitoring water discharge and floodplain connectivity for the northern Andes utilizing satellite data: a tool for river planning and science-based decision-making. *J. Hydrol.* 586, 124887. <https://doi.org/10.1016/j.jhydrol.2020.124887>.

Richey, J.E., Hedges, J.I., Devol, A.H., Quay, P.D., Victoria, R., Martinelli, L., Forsberg, B.R., 1990. Biogeochemistry of carbon in the Amazon River. *Limnol. Oceanogr.* 35, 352–371. <https://doi.org/10.4319/lo.1990.35.2.0352>.

Richey, J.E., Melack, J.M., Aufdenkampe, A.K., Ballester, V.M., Hess, L.L., 2002. Outgassing from Amazonian rivers and wetlands as a large tropical source of atmospheric CO₂. *Nature* 416, 617–620. <https://doi.org/10.1038/416617a>.

Rodriguez-Alvarez, N., Podest, E., Jensen, K., McDonald, K.C., 2019. Classifying inundation in a tropical wetlands complex with GNSS-R. *Remote Sens.* 11, 1053. <https://doi.org/10.3390/rs11091053>.

Rosenqvist, A., Forsberg, B.R., Pimentel, T., Rauste, Y.A., Richey, J.E., 2002. The use of spaceborne radar data to model inundation patterns and trace gas emissions in the Central Amazon floodplain. *Int. J. Remote Sens.* 23, 1303–1328. <https://doi.org/10.1080/01431160110092911>.

Rosenqvist, J., Rosenqvist, A., Jensen, K., McDonald, K., 2020. Mapping of maximum and minimum inundation extents in the Amazon Basin 2014–2017 with ALOS-2 PALSAR-2 ScanSAR time-series data. *Remote Sens.* 12, 1326. <https://doi.org/10.3390/rs12081326>.

Rossetti, D.F., Gribel, R., Rennó, C.D., Cohen, M.C.L., Moulatlet, G.M., de Cordeiro, C.L.O., do Rodrigues, E.S.F., 2017a. Late Holocene tectonic influence on hydrology and vegetation patterns in a northern Amazonian megafan. *Catena* 158, 121–130. <https://doi.org/10.1016/j.catena.2017.06.022>.

Rossetti, D.F., Valeriano, M.M., Gribel, R., Cohen, M.C.L., Tatumi, S.H., Yee, M., 2017b. The imprint of Late Holocene tectonic reactivation on a megafan landscape in the northern Amazonian wetlands. *Geomorphology* 295, 406–418. <https://doi.org/10.1016/j.geomorph.2017.07.026>.

Rudorff, C.M., Melack, J.M., Bates, P.D., 2014. Flooding dynamics on the lower Amazon floodplain: 1. Hydraulic controls on water elevation, inundation extent, and river-floodplain discharge. *Water Resour. Res.* 50, 619–634. <https://doi.org/10.1002/2013WR014091>.

Ruf, C.S., Chew, C., Lang, T., et al., 2018. A new paradigm in earth environmental monitoring with the CYGNSS small satellite constellation. *Sci. Rep.* 8, 8782. <https://doi.org/10.1038/s41598-018-27127-4>.

Santos, J.O.S., Nelson, B.W., Giovannini, C.A., 1993. *Corpos de areia sob leitos abandonados de grandes rios*. Ciéncia Hoje 16, 22–25.

Saunois, M., Stavert, A.R., Poulter, B., Bousquet, P., Canadell, J.G., Jackson, R.B., Raymond, P.A., Dlugokencky, E.J., Houweling, S., Patra, P.K., Ciais, P., Arora, V.K., Bastviken, D., Bergamaschi, P., Blake, D.R., Braisford, G., Bruhwiler, L., Carlson, K.M., Carroll, M., Castaldi, S., Chandra, N., Crevoisier, C., Crill, P.M., Covey, K., Curry, C.L., Etiöpe, G., Frankenberger, C., Gedney, N., Hegglin, M.I., Höglund-Isaksson, L., Hugelius, G., Ishizawa, M., Ito, A., Janssens-Maenhout, G., Jensen, K.M., Joos, F., Kleinen, T., Krummel, P.B., Langenfelds, R.L., Laruelle, G.G., Liu, L., Machida, T., Maksyutov, S., McDonald, K.C., McNorton, J., Miller, P.A., Melton, J.R., Morino, I., Müller, J., Murguia-Flores, F., Naik, V., Niwa, Y., Noce, S., O'Doherty, S., Parker, R.J., Peng, C., Peng, S., Peters, G.P., Prigent, C., Prinn, R., Ramonet, M., Regnier, P., Riley, W.J., Rosentreter, J.A., Segers, A., Simpson, I.J., Shi, H., Smith, S.J., Steele, L.P., Thornton, B.F., Tian, H., Tohjima, Y., Tubiello, F.N., Tsuruta, A., Viovy, N., Voulgarakis, A., Weber, T.S., van Weele, M., van der Werf, G.R., Weiss, R.F., Worthy, D., Wunch, D., Yin, Y., Yoshida, Y., Zhang, W., Zhang, Z., Zhao, Y., Zheng, B., Zhu, Qing, Zhu, Qian, Zhuang, Q., 2020. The global methane budget 2000–2017. *Earth Syst. Sci. Data* 12, 1561–1623. <https://doi.org/10.5194/essd-12-1561-2020>.

Schöngart, J., Wittmann, F., Faria de Resende, A., Assahira, C., Sousa Lobo, G., Rocha Duarte Neves, J., Rocha, M., Biem Mori, G., Costa Quaresma, A., Oreste Demarchi, L., Weiss Albuquerque, B., Oliveira Feitoza, Y., Silva Costa, G., Vieira Feitoza, G., Machado Durgante, F., Lopes, A., Trumbore, S.E., Sanna Freire Silva, T., Steege, H., Val, A.L., Junk, W.J., Piedade, M.T.F., 2021. The shadow of the Balbina dam: a synthesis of over 35 years of downstream impacts on floodplain forests in Central Amazonia. *Aquat. Conserv. Mar. Freshwat. Ecosyst.* 31, 1117–1135. <https://doi.org/10.1002/aqc.3526>.

Schroeder, R., McDonald, K., Chapman, B., Jensen, K., Podest, E., Tessler, Z., Bohn, T., Zimmermann, R., 2015. Development and evaluation of a multi-year fractional surface water data set derived from active/passive microwave remote sensing data. *Remote Sens.* 7, 16688–16732. <https://doi.org/10.3390/rs71215843>.

Schumann, G.J.P., Stompoulis, D., Smith, A.M., Sampson, C.C., Andreadis, K.M., Neal, J.C., Bates, P.D., 2016. Rethinking flood hazard at the global scale. *Geophys. Res. Lett.* 43, 10249–10256. <https://doi.org/10.1002/2016GL070260>.

Silva, T.S.F., Melack, J.M., Novo, E.M.L.M., 2013. Responses of aquatic macrophyte cover and productivity to flooding variability on the Amazon floodplain. *Glob. Chang. Biol.* 19, 3379–3389. <https://doi.org/10.1111/gcb.12308>.

Silva, M.V., Paris, A., Calmant, S., Cândido, L.A., da Silva, J.S., 2018. Relationships between Pacific and Atlantic Ocean sea surface temperatures and water levels from satellite altimetry data in the Amazon rivers. *Br. J. Water Resour.* 23 <https://doi.org/10.1590/2318-0331.231820170148>.

Sippel, S.J., Hamilton, S.K., Melack, J.M., Novo, E.M.M., 1998. Passive microwave observations of inundation area and the area/stage relation in the amazon river floodplain. *Int. J. Remote Sens.* 19, 3055–3074. <https://doi.org/10.1080/014311698214181>.

Siqueira, V.A., Paiva, R.C.D., Fleischmann, A.S., Fan, F.M., Ruhoff, A.L., Pontes, P.R.M., Paris, A., Calmant, S., Collischonn, W., 2018. Toward continental hydrologic-hydrodynamic modeling in South America. *Hydrol. Earth Syst. Sci.* 22, 4815–4842. <https://doi.org/10.5194/hess-22-4815-2018>.

Sorribas, M.V., Paiva, R.C.D., Melack, J.M., Bravo, J.M., Jones, C., Carvalho, L., Beighley, E., Forsberg, B., Costa, M.H., 2016. Projections of climate change effects on discharge and inundation in the Amazon basin. *Clim. Chang.* 136, 555–570. <https://doi.org/10.1007/s10584-016-1640-2>.

Staver, A.C., Archibald, S., Levin, S.A., 2011. The global extent and determinants of savanna and forest as alternative biome states. *Science* 334, 230–232. <https://doi.org/10.1126/science.1210465>.

Taylor, C.M., Prigent, C., Dadson, S.J., 2018. Mesoscale rainfall patterns observed around wetlands in sub-Saharan Africa. *Q. J. R. Meteorol. Soc.* 144, 2118–2132. <https://doi.org/10.1002/qj.3311>.

Towner, J., Cloke, H.L., Zsoter, E., Flaming, Z., Hoch, J.M., Bazo, J., Coughlan de Perez, E., Stephens, E.M., 2019. Assessing the performance of global hydrological models for capturing peak river flows in the Amazon basin. *Hydrol. Earth Syst. Sci.* 23, 3057–3080. <https://doi.org/10.5194/hess-23-3057-2019>.

Trigg, M.A., Wilson, M.D., Bates, P.D., Horritt, M.S., Alsdorf, D.E., Forsberg, B.R., Vega, M.C., 2009. Amazon flood wave hydraulics. *J. Hydrol.* 374, 92–105. <https://doi.org/10.1016/j.jhydrol.2009.06.004>.

Trigg, M.A., Birch, C.E., Neal, J.C., Bates, P.D., Smith, A., Sampson, C.C., Yamazaki, D., Hirabayashi, Y., Pappenberger, F., Dutra, E., Ward, P.J., Winsemius, H.C., Salamon, P., Dottori, F., Rudari, R., Kappes, M.S., Simpson, A.L., Hadzilacos, G., Fewtrell, T.J., 2016. The credibility challenge for global fluvial flood risk analysis. *Environ. Res. Lett.* 11, 094014. <https://doi.org/10.1088/1748-9326/11/9/094014>.

Ward, N.D., Bianchi, T.S., Medeiros, P.M., Seidel, M., Richey, J.E., Keil, R.G., Sawakuchi, H.O., 2017. Where carbon goes when water flows: carbon cycling across the aquatic continuum. *Front. Mar. Sci.* 4, 1–27. <https://doi.org/10.3389/fmars.2017.00007>.

Wilson, M.D., Bates, P., Alsdorf, D., Forsberg, B., Horritt, M., Melack, J., Frappart, F., Famiglietti, J., 2007. Modeling large-scale inundation of Amazonian seasonally flooded wetlands. *Geophys. Res. Lett.* 34, 4–9. <https://doi.org/10.1029/2007GL030156>.

Wongchuig, S.C., de Paiva, R.C.D., Espinoza, J.C., Collischonn, W., 2017. Multi-decadal hydrological retrospective: case study of Amazon floods and droughts. *J. Hydrol.* 549, 667–684. <https://doi.org/10.1016/j.jhydrol.2017.04.019>.

Wongchuig, S.C., de Paiva, R.C.D., Siqueira, V., Collischonn, W., 2019. Hydrological reanalysis across the 20th century: a case study of the Amazon Basin. *J. Hydrol.* 570, 755–773. <https://doi.org/10.1016/j.jhydrol.2019.01.025>.

Wongchuig, S.C., Paiva, R.C.D., Biancamaria, S., Collischonn, W., 2020. Assimilation of future SWOT-based river elevations, surface extent observations and discharge estimations into uncertain global hydrological models. *J. Hydrol.* 590, 125473 <https://doi.org/10.1016/j.jhydrol.2020.125473>.

Wu, J., Lakshmi, V., Wang, D., Lin, P., Pan, M., Cai, X., Wood, E.F., Zeng, Z., 2020. The reliability of global remote sensing evapotranspiration products over Amazon. *Remote Sens.* 12, 2211. <https://doi.org/10.3390/rs12142211>.

Yamazaki, D., Kanae, S., Kim, H., Oki, T., 2011. A physically based description of floodplain inundation dynamics in a global river routing model. *Water Resour. Res.* 47, 1–21. <https://doi.org/10.1029/2010WR009726>.

Yamazaki, D., Sato, T., Kanae, S., Hirabayashi, Y., Bates, P.D., 2014. Regional flood dynamics in a bifurcating mega delta simulated in a global river model. *Geophys. Res. Lett.* 41, 3127–3135. <https://doi.org/10.1002/2014GL059744>.

Yamazaki, D., Trigg, M.A., Ikeshima, D., 2015. Development of a global ~90m water body map using multi-temporal Landsat images. *Remote Sens. Environ.* 171, 337–351. <https://doi.org/10.1016/j.rse.2015.10.014>.

Yamazaki, D., Ikeshima, D., Tawatari, R., Yamaguchi, T., O'Loughlin, F., Neal, J.C., Sampson, C.C., Kanae, S., Bates, P.D., 2017. A high-accuracy map of global terrain elevations. *Geophys. Res. Lett.* <https://doi.org/10.1002/2017GL072874>.

Zhang, Z., Poulter, B., Fluet-Chouinard, E., Jensen, K., McDonald, K., Hugelius, G., Gumbrecht, T., Carroll, M., Prigent, C., Bartsch, A., 2020. Development and evaluation of the global wetland area and dynamics for methane modeling dataset (WAD2M). *Earth Syst. Sci.* 1–50. <https://doi.org/10.5194/esd-2020-262>. Data in review.

Zhou, X., Prigent, C., Yamazaki, D., 2021. Toward improved comparisons between land-surface-water-area estimates from a global river model and satellite observations. *Water Resour. Res.* 57 <https://doi.org/10.1029/2020WR029256> e2020WR029256.

Zubieta, R., Getirana, A., Espinoza, J.C., Lavado, W., 2015. Impacts of satellite-based precipitation datasets on rainfall-runoff modeling of the Western Amazon basin of Peru and Ecuador. *J. Hydrol.* 528, 599–612. <https://doi.org/10.1016/j.jhydrol.2015.06.064>.

Zubieta, R., Getirana, A., Espinoza, J.C., Lavado-Casimiro, W., Aragon, L., 2017. Hydrological modeling of the Peruvian-Ecuadorian Amazon Basin using GPM-IMERG satellite-based precipitation dataset. *Hydrol. Earth Syst. Sci.* 21, 3543–3555. <https://doi.org/10.5194/hess-21-3543-2017>.

Zubieta, R., Saavedra, M., Espinoza, J.C., Ronchail, J., Sulca, J., Drapeau, G., Martin-Vide, J., 2019. Assessing precipitation concentration in the Amazon basin from different satellite-based data sets. *Int. J. Climatol.* 39, 3171–3187. <https://doi.org/10.1002/joc.6009>.